Cheloni Daniele (Orcid ID: 0000-0002-0958-2129)
Falcucci Emanuela (Orcid ID: 0000-0003-3716-7392)

Half-graben rupture geometry of the 30 October 2016 M_W 6.6 Mt. Vettore-Mt. Bove earthquake, central Italy

D. Cheloni[1], E. Falcucci[1], and S. Gori[1]

[1]Istituto Nazionale di Geofisica e Vulcanologia, Via di Vigna Murata 605, 00143 Rome, Italy

Corresponding author: Daniele Cheloni (daniele.cheloni@ingv.it)

Key Points:

- We revisit the rupture geometry of the M_W 6.6 30 October 2016 earthquake in central Italy.
- The earthquake ruptured both the master normal fault system and the antithetic faults on the opposite side of the Castelluccio plain.
- No significant coseismic slip on faults alternative to the master and antithetic faults is necessary to reproduce the surface displacements.

This article has been accepted for publication and undergone full peer review but has not been through the copyediting, typesetting, pagination and proofreading process which may lead to differences between this version and the Version of Record. Please cite this article as doi: 10.1029/2018JB015851

Abstract

Existing models for the rupture geometry and slip distribution associated with the 30 October M_W 6.6 Mt. Vettore-Mt. Bove earthquake in central Italy show significant dissimilarities. Indeed, due to the quite complicated observed deformation pattern, the activation of a complex multi-fault structure during a single seismic event was invoked. In this study, we explore different rupture scenarios and we develop a robust model of the rupture process of the 30 October earthquake, designed from new field observations, aftershocks distribution and static coseismic offsets including new near-field survey-mode GPS measurements, regional GPS observations, InSAR interferograms and static displacements derived from strong-motion stations. Our preferred best-fit model involves the simultaneously rupture of the master Mt. Vettore-Mt. Bove normal fault and of at least two secondary antithetic faults (as they significantly contributed to the total deformation field), which overall describe a "simple conceptual" half-graben normal fault system, and whose arrangement fits the geological, seismological and the coseismic evidence of surface faulting. Notably, our model fits the geometry of seismogenic structures defined prior to the 2016-2017 seismic sequence by field Quaternary geological observations. In addition, no significant coseismic slip on faults alternative to the master and antithetic faults is necessary to explain the observed surface displacements during the 30 October Mt. Vettore-Mt. Bove earthquake.

1 Introduction

During major earthquakes complex fault networks composed of fault segments and secondary splays of diverse orientations can be involved in the rupture process. Indeed, although earthquakes are thought to occur along a single fault, increasing evidence from both field observations and numerical models point out active slip on multiple faults during a single earthquake [e.g., *Resor et al.,* 2005; *Wang et al.,* 2010; *Fletcher et al., 2016; Hamling et al.,* 2017]. In this context, the increasing availability of spatially rich measurements of surface deformation obtained by analysis of global navigation satellite system (GNSS) observations and of interferometric synthetic aperture radar (InSAR) images have significantly improved the description of earthquake source mechanisms, offering researchers the opportunity to develop increasingly complex geometric models of earthquakes rupture.

However, geodetic inversion solutions are intrinsically non-unique and unstable due to trade-offs between model parameters, especially in geometrically complex tectonic settings. Complex multi-fault models supposed only basing on the minimization of the residuals of a certain mathematical model are therefore not a "guarantee" of a complete and reliable analysis of the structural framework associated with the considered seismic event. For this reason, it is essential to consider other independent information given, for example, by surface ruptures, long-term geology and aftershocks distribution to constrain some model parameters and to better define the geometry of the fault network in the activated crustal volume. An improved understanding of an active fault system geometry is important to give a more accurate contribution to the seismotectonic analysis and for a better understanding of the earthquake rupture process.

In this context, we revisit the 30 October 2016 M_W 6.6 Mt. Vettore-Mt. Bove earthquake (also called the "Norcia earthquake"), which represents the largest normal faulting seismic event in Italy, and worldwide, in terms of unprecedented set of modern geophysical techniques of observation. The slip in this earthquake was quite complicated and many different scenarios have already been invoked by various authors working on field, geodetic and seismological data. In particular, it has been suggested that a gently NW-dipping

structure which is oblique to the strike of the primary SW-dipping Mt. Vettore-Mt. Bove normal fault was involved in the seismic sequence as a reactivated (in normal sense) thrust fault or as a normal fault bounding the Castelluccio basin to the south. Here, we present new geodetic modelling from the sequence integrating it with the coseismic evidence of surface faulting, aftershock relocations and long-term geological data to mitigate problems of non-uniqueness associated with the individual datasets. To this end, we reinverted the already published geodetic data related to the 30 October event (i.e., regional GPS observations and coseismic InSAR interferograms), integrating them with new near-field coseismic displacements relative to a local temporary GPS network set across the fault trace of the Mt. Vettore-Mt. Bove fault system, and with the static coseismic offsets derived by strong-motion data of the closest seismic stations. The results of the inversions allow us to explore the structures involved in the coseismic dislocation and to discuss the feasibility of a "simple conceptual" half-graben dislocation model *versus* a more complex fault array, i.e., invoking the primary simultaneous multi-fault rupture of both normal fault systems and cross-structures, in reconciling the earthquake dislocation. Hence, our results demonstrate the significant advantage of considering independent information given by geology and seismicity along with space geodesy to define the geometry, as well as the slip distribution of the activated fault network.

2 The 2016-2017 Central Italy Earthquake Sequence

The 30 October 2016 M_W 6.6 earthquake is the mainshock of the seismic sequence that started to affect central Italy since 24 August 2016 with the M_W 6.2 Amatrice earthquake, followed by the 26 October M_W 5.9 Visso event, and then culminated with 30 October mainshock (Figure 1). The bulk of geological [e.g., *EMERGEO Working Group,* 2016; *Falcucci et al.,* 2016; *Galadini et al.,* 2017; *Pizzi et al.,* 2017; *Civico et al.,* 2018; *Villani et al.,* 2018], seismological [*Tinti et al.,* 2016; *Chiaraluce et al.,* 2017; *Papadopoulos et al.,* 2017; *Pizzi et al.,* 2017; *Scognamiglio et al.,* 2018] and geodetic [*Lavecchia et al.,* 2016; *Cheloni et al.,* 2017; *Huang et al.,* 2017; *Xu et al.,* 2017; *Walters et al.,* 2018; *Wang et al.,* 2018] data agreed in attributing the whole sequence to the progressive rupture of a fault affecting the eastern sector of the Amatrice basin and of the Mt. Vettore-Mt. Bove normal fault system, that is, two major ~NW-SE striking extensional tectonic structures of the central Apennines (Figure 1).

The Quaternary activity of these fault systems determined the formation of half-graben structures, with the main fault located on the eastern side and dipping to the SW. In particular, the Mt. Vettore-Mt. Bove (MVB) fault was considered a roughly 20 km-long active tectonic structure before the 2016-2017 seismic sequence and the surface manifestation of magnitude 6.5-7 earthquakes [e.g., *Galadini & Galli,* 2000, 2003], as it shows evidence of late Pleistocene-Holocene activity [e.g., *Cello et al.* 1997; *Galadini & Galli,* 2003; *Pizzi & Galadini,* 2009]. As for the late Holocene slip history, the MVB fault last event of activation predates the past millennium and it was thus considered as a seismic gap [*Galadini & Galli,* 2003]. In addition, major NNE-SSW striking faults represent the pre-existing cross-structures with the respect to the trend of the Quaternary extensional faulting (Figure 1). In the study area, in particular, the major inherited structure is the Olevano-Antrodoco-Sibillini Mts. thrust (OAST) ramp. According to some authors [e.g., *Pizzi & Galadini,* 2009] the NNE-SSW striking ramp of the OAST could represent the expression of an inverse reactivation of the high-angle Ancona-Anzio Line that represents in turn a regional Mesozoic paleogeographic boundary. The interaction between the Quaternary extensional fault systems and the inherited thrusts (in terms of segmenting the lateral extension of the active normal faults or of a possible active role of the thrust faults during the seismic sequence) is still

under debate [*Pizzi & Galadini,* 2009; *Bonini et al.,* 2016; *Pizzi et al.,* 2017; *Chiarabba et al.,* 2018; *Scognamiglio et al.,* 2018].

A number of studies dealt with coseismic slip models for each of the three mainshocks of the 2016-2017 central Italy seismic sequence. All of them, made by inverting geodetic data [*Lavecchia et al.,* 2016; *Cheloni et al.,* 2017; *Huang et al.,* 2017; *Xu et al.,* 2017; *Walters et al.,* 2018; *Wang et al.,* 2018], seismological data [*Tinti et al.,* 2016; *Chiaraluce et al.,* 2017; *Papadopoulos et al.,* 2017; *Pizzi et al.,* 2017] or combinations of them [*Liu et al.,* 2017; *Cirella et al.,* 2018; *Scognamiglio et al.,* 2018] described, at first order, the activation of a ~NW-SE striking and SW dipping normal fault system. As for the 30 October M_W 6.6 event, in particular, the models published to date [*Cheloni et al.,* 2017; *Chiaraluce et al.,* 2017; *Liu et al.,* 2017; *Papadopoulos et al.,* 2017; *Pizzi et al.,* 2017; *Xu et al.,* 2017; *Scognamiglio et al.,* 2018; *Walters et al.,* 2018; *Wang et al.,* 2018] define an approximately N150°-160° striking normal fault, in agreement with the direction of active extension in this sector of the Apennines [e.g., *D'Agostino,* 2014; *Cheloni et al.,* 2016a; *Devoti et al.,* 2017], and whose surface projection corresponds to the trace of the MVB fault system, along which surface faulting indeed occurred (Figure 1) [*Galadini et al.,* 2017; *Civico et al.,* 2018; *Villani et al.,* 2018]. Moreover, by using a local low-cost GNSS network, *Wilkinson et al.* [2017] showed that the observed surface ruptures resulted by the dynamic earthquake slip reaching the surface, since they occurred rapidly with respect to the hypocenter origin time. According to the authors, this means that the observed surface ruptures are primary surface faulting (directly related to the seismogenic fault), likely ruling out significant non-tectonic or secondary component to the 30 October coseismic surface rupture, e.g., shaking induced gravitational processes, or a passive reactivation of secondary faults, as primary driving mechanism.

However, because of the relatively complicated pattern of deformation caused by this earthquake, the coseismic slip models proposed to date show some dissimilarities in terms of precise fault location, fault size, fault dip angle and slip distribution along the ruptured plane. Moreover, some modelling results show some persistent residuals in the Norcia area and in the southern part of the Castelluccio plain, where the geological study of *Pierantoni et al.* [2013] mapped antithetic structures on the western side of the Pian Grande basin (Figure 2), while other authors suggested the presence of oblique faults bounding the basin (Pian Piccolo) to the south [*Coltorti & Farabollini, 1995*]. For this reason, some authors [*Cheloni et al.,* 2017; *Chiaraluce et al.,* 2017; *Pizzi et al.,* 2017; *Scognamiglio et al.,* 2018; *Valerio et al.,* 2018; *Walters et al.,* 2018] suggested that the assumption that only a single planar fault slipped in the 30 October earthquake may not be exhaustive. In particular, *Pizzi et al.* [2017] and *Chiarabba et al.* [2018] issued that the oblique ramp of the low-angle OAST may have played a role in differentiating the sources of the 24 August and of the 30 October events. The possible secondary coseismic contribution of an oblique low-angle fault to the 30 October rupture event has been tested in the geodetic modelling of *Cheloni et al.* [2017] who, nonetheless, defined this hypothesis as less probable than the coseismic activation of a major MVB antithetic fault plane. In addition, according to the 2D finite elements modelling of InSAR measurements of *Valerio et al.* [2018], the presence of an antithetic fault zone is necessary to fully model the observed coseismic deformation pattern as depicted by InSAR measurements. On the contrary, *Scognamiglio et al.* [2018] modelled local strong-motion and GPS data and proposed that a large amount of coseismic slip of the 30 October mainshock took place along a similar secondary low-angle fault, oblique to the MVB fault system, and possibly associated to a deep portion of the NNE-trending OAST ramp. Finally, also in a recent study, *Walters et al.* [2018] have investigated the possibility that an additional normal

fault cross-cutting the southern rim of the Castelluccio plain has slipped during the 30 October earthquake, together with a number of antithetic and synthetic splays of the Mt. Vettore-Mt. Bove fault system.

In terms of seismicity, relocated aftershocks recorded three months following the 24 August earthquake [*Chiaraluce et al.,* 2017] revealed clusters of events that well illuminate antithetic NE dipping normal faults, rooting downdip to the MVB master fault and ending up-dip against the Norcia fault. In particular, a major antithetic fault, located northward of the OAST in the area of the northern patch of the 24 August Amatrice event, is strongly delineated by aftershock distribution. This fault was also probably partially activated by a M_W 5.4 aftershock, with a normal focal mechanism consistent with the trend of the MVB fault system, that occurred almost one hour after the Amatrice mainshock close to the Norcia town and nucleating at the intersection with the main fault plane [*Scognamiglio et al.,* 2016]. Conversely, seismicity does not suggest any unequivocal low-angle structure supposedly related to the inherited OAST ramp, especially where this structure was tentatively located by the above-mentioned authors to explain possible rupture complexities. Furthermore, according to *Chiaraluce et al.* [2017], the presumable low dip angle (i.e., deduced from the geometry at surface of the OAST) of this compressional structure would not be consistent with the spatial-temporal evolution of the seismic activity, which instead would suggest an almost vertical separation between the MVB and the Amatrice fault.

In our modelling, we therefore interpret the alignments of aftershocks described above as a typical half-graben structure (Figure 3). However, we also consider a number of different coseismic scenarios for the 30 October mainshock (i.e., a half-graben dislocation model or a more complex fault array invoking the primary simultaneous multi-fault rupture of both normal fault systems and inherited cross-structures), reflecting the different seismotectonics interpretations, the dips and trends observed in the aftershock relocations, the long-term surface geological data as well as the coseismic evidence of surface faulting along all of the activated segments and splays. The purpose is to obtain a dislocation model that improves the fit to the geodetic data while considering the observations of surface rupturing and reflecting the trends observed in the aftershock relocations. These different datasets all contribute to the complete definition of the earthquake source characteristics. These models will be presented and discussed in section 4.

3 Data

We use a comprehensive geodetic dataset composed of regional GPS measurements at 37 sites belonging to the Istituto Nazionale di Geofisica e Vulcanologia [*INGV Working Group "GPS Geodesy",* 2016], CaGeoNet [*Anzidei et al.,* 2005; *Galvani et al.,* 2012] and to the Istituto Geografico Militare (IGM, www.igmi.org) networks, of 5 local survey-mode GPS observations in the near-field of the MVB fault trace [*De Guidi et al.,* 2017], 6 static displacements derived from the closest strong-motion stations [*Zimmaro et al.,* 2018], the ALOS-2 coseismic ascending interferogram relevant to the 30 October event [*Cheloni et al.,* 2017] and the Sentinel-1 descending interferogram covering both the 26 and 30 October earthquakes [*Walters et al.,* 2018]. This combination of data provides good coverage in both near- and far-field of the 30 October earthquake. In addition, we collected field evidence in the aftermath of the event all along the main MVB fault system and also along the major synthetic and antithetic splays as surveyed in the field.

3.1 Field Observations

The three mainshocks of the sequence caused surface faulting along the ~28 km long MVB fault system (Figures 1 and 4) [*Galadini et al.,* 2017; *Civico et al.,* 2018; *Villani et al.,* 2018]. The 30 October event, in particular, ruptured the ground surface along most of the splays of the seismogenic structure (maximum offset ~1.5 m along the easternmost fault splay; Figure 4b). The major synthetic splays affecting the SW slopes of the Mt. Vettore and Mt. Bove showed cm-to-m scale vertical offsets (Figure 4c). Field surveys also revealed that at least two major antithetic splays underwent surface faulting (Figure 1). The main trace of these structures was already mapped in the geological study of *Pierantoni et al.* [2013].

The northernmost of the antithetic faults bounds to the east the Piano Perduto depression, located ~3 km north of Castelluccio (hereafter named as Piano Perduto antithetic fault and also called as the "Valle Infante fault" in *Civico et al.* [2018]). A maximum of 60 cm surface offset was seen along it, for ~1.5-3 km in length (Figure 4d). The southernmost antithetic splay crosses the reliefs that separate the Castelluccio depression (named as Piano Grande) from the Norcia plain to the west (hereafter named as Rifugio Perugia antithetic fault). We found evidence of cm scale surface ruptures along different portion of this structure (Figures 4e and 4f). In particular, near the Rifugio Perugia (RIFP GPS station, Figure 4f), that is a small hotel severely damaged by the 30 October earthquake, a several meters-long ground cracks with ~5 cm vertical offset (east side lowered) were seen aligned along the fault. Towards the south, the antithetic fault and some associated minor shear planes intersect the road that leads from Forca Canepine to Norcia, where small fractures aligned with fault crossed the pavement are evident (Figure 4e, inset). In addition, our observations indicate that these structures have a very wide deformation zone made of a number of high-angle shear planes that experienced a complex kinematic history. In particular, extensional kinematics superposes to transpressive-reverse kinematics related to the compressive Pliocene tectonic phase (Figures S1 and S2). Finally, and more importantly, in correspondence with the southern end of the deformation zone, the reinforced concrete San Benedetto tunnel that connects the Norcia plain with Arquata del Tronto underwent several centimeters displacement (the infrastructure in presently under restoration) after the 30 October event. Damage occurred ~1 km from the western entrance of the tunnel (Figures 1 and 2) and involved both the pavement and the vault in a narrow belt about 60 m wide [*Galli et al.,* 2017]. The coincidence with the trace of minor shear planes associated to the southernmost antithetic fault (Figure 2) suggests that the tunnel damage has been caused by the coseismic activation of this structure.

Hence, together with the main synthetic splays of the MVB fault system, an unneglectable slip occurred also along at least the two described antithetic faults. This piece of evidence deserves to be considered in the source modelling, to explore all of the possible contributions and complexities in the coseismic deformation pattern associated to the activated structures.

3.2 Geodetic Observations

We use the GPS measurements of coseismic displacements from *Cheloni et al.* [2017], which reveal a general relative normal motion SW-NE oriented across the MVB fault system (Figure 5). In addition, we also use the static coseismic displacements measured by a local GPS network deployed across the trace of the main fault [*De Guidi et al.,* 2017], which had never been previously used in the source modelling of this earthquake. The latter GPS measurements provide another independent constraint on the fault location and coseismic slip. Finally, the static displacements derived from six strong-motion (SM-derived) stations [*Zimmaro et al.,* 2018] were integrated in the inversion to complement the GPS

measurements (Figure 5). The largest horizontal and vertical static offsets were measured in correspondence of Castelluccio, where both GPS and SM-derived displacements show > 50 cm movement toward southwest and a subsidence reaching up ~90 cm, in agreement with InSAR data (see Figure S3 in *Cheloni et al.* [2017]).

In addition, we use also InSAR data to obtain the coseismic deformation of the 30 October earthquake along the satellite line-of-sight (LOS). In particular, a number of combinations of ascending and descending interferograms involving different sensors are available for 2016-2017 central Italy earthquake sequence [e.g., *Cheloni et al.,* 2017; *Walters et al.,* 2018]. However, almost the published interferograms measure only the cumulative ground displacement due to both the 26 October Visso and the 30 October earthquakes, spanning also a variable amount of post-seismic deformation following the preceding 24 August Amatrice event. Thus, to minimize the effects of possible post-seismic deformation following the preceding Amatrice earthquake, we only use in the modelling the interferograms that contain the shortest time period before the October events. In particular, we exploited the ascending ALOS-2 interferogram which involves the 28 October 2016/11 November 2016 acquisitions and relevant only to the 30 October event [*Cheloni et al.,* 2017] and the descending Sentinel-1 (SENT-1) interferogram, which involves the 26 October 2016/1 November 2016 acquisitions. This allows to measure the cumulative ground displacement due to both the 26 and 30 October earthquakes, but not that of the Amatrice post-seismic deformation [*Walters et al.,* 2018]. To use the Sentinel-1 data in our inversion scheme, we simply cut out the northern part of the interferogram, as the 26 October Visso event does not affect the southern part of the 30 October rupture [*Walters et al.,* 2018].
In the interferograms (Figure 6), apart from the largest LOS signal extending along the NNW-SSE direction from Ussita to the southern edge of the Castelluccio plain (with maximum negative LOS of ~70-100 cm; negative LOS values represent increasing distance from the satellite), a smaller NNW-SSE deformation lobe in the ascending interferogram (LOS values ~50 cm) appears to the west of the main fault trace (along the southwestern margin of the Castelluccio plain), and right to the east of the Rifugio Perugia antithetic fault as revealed by our field surveys (see Section 3.1). Finally, the area of Norcia shows positive LOS values (~25 cm) corresponding to a combination of west-southwestward displacements and uplift, as expected in this area of the hanging wall of the main normal fault system.

4 Inversion of Geodetic Data

In this section, we illustrate the results of the inversion for variable slip on a number of different fault networks corresponding to 1) "simple conceptual" half-graben rupture scenarios and to 2) more complex fault arrangement rupture scenarios, that is, invoking the simultaneous rupture of both normal fault systems and transverse structures, and we discuss to what extent the simplest or more complex scenario is required by the data. We use the same inversion scheme as in *Cheloni et al.* [2016b], which adopted rectangular dislocations in an elastic, homogeneous and isotropic half-space [*Okada*, 1985]. We solve for the two components of slip, i.e. strike- and dip-slip, for each fault patch and regularize the inversions using a Laplacian operator, forcing slip to be zero on the boundary of the fault planes, except for the upper edge of the master fault to allow surficial slip if any. Although the bulk of evidence constrains the fault geometry of the main MVB fault, we inferred its optimal geometry iterating by grid searching over strikes, locations and dips of the fault plane jointly inverting the GPS, SM-derived and InSAR displacements. Additional terms (i.e., linear ramp for InSAR displacements) were also included in the modelling, and relative weights were applied to properly combine the different data sets, considering the much larger number of InSAR data points compared to the other measurements (Figure S3). The inversions were

carried out using a bounded-values weighted least-squares algorithm [*Stark and Parker*, 1995], and the amount of smoothing was adjusted to trade-off with data misfit reduction and model roughness (Figure S4).

Determining an initial fault model is quite straightforward, owing to the measured displacement patterns and to the coseismic evidence that slip of the 30 October earthquake reached the surface both along the main MVB fault system [*Galadini et al.,* 2017; *Wilkinson et al.,* 2017; *Civico et al.,* 2018; *Villani et al.,* 2018] and along the two described antithetic faults (Figure 1). Thus, using relocated aftershocks, geodetic displacements and field measurements we imaged the details of the initial fault network associated to the 30 October 2016 Mw 6.6 Mt. Vettore-Mt. Bove earthquake. Our interpreted fault network consists in different fault segments including (Figure 3): 1) the master MVB normal fault system that strikes NW-SE and dips towards SW; 2) a more steeply main blind antithetic fault extending along strike from the epicenter to the southern part of the Castelluccio plain; 3) minor hanging wall synthetic and antithetic splays (two of them underwent surface faulting, see Section 2.1); and 4) an almost flat feature 8-10 km deep, confining at depth almost the entire fault system. In summary, we added antithetic and synthetic splay faults to the master fault system to model failure of multiple fault segments that describe a typical half-graben structure [*Bruhn & Schultz*, 1996]. As regard the (4) deep flat feature, it may represent a major rheological/mechanical transition where the stress concentrates between high-angle normal faults and a basal low-angle discontinuity characterized by a creeping behavior as observed in other portions of the Central Apennines [*Valoroso et al.,* 2013]. In addition, structural and geological studies [e.g., *Pizzi & Galadini*, 2009] suggest the existence in the activated volume of inherited compressive structures oblique to the main normal fault system, that is the OAST ramp. The seismicity distribution does not enlighten any unequivocal structure compatible with the inherited OAST at hypocentral depth. Only in the footwall of the main MVB fault system, at shallower depths (1-3 km) but northward of the 30 October epicenter, small magnitude earthquakes seem to nucleate on a shallow portion of the OAST (see sections 7-9 in Figure 3b of *Chiaraluce et al.* [2017]). Nevertheless, we tested also the possibility that a NE-SW striking and NW dipping structure, oblique to the main MVB fault system might have been involved by the 30 October earthquake.

4.1 Half-Graben Rupture Scenarios

The best-fitting fault model composed of a single planar segment (F1) is a fault plane striking N159° and dipping 38° SW (Figure 7a), with geometry similar to that used by *Cheloni et al.* [2017], *Xu et al.* [2017] and *Walters et al.* [2018]. The surface trace of our optimized F1 modelled segment also fits the mean mapped trace of the MVB fault system (Figure 7). However, using the best-fitting single dislocation (1-fault model), the final fit to the geodetic data is not optimal, with important residuals in the Norcia area and in the southern part of the Castelluccio plain (Figures 5a, 5b, 6a-6c and 6j-6l), as already depicted or suggested in previous studies [*Cheloni et al.,* 2017; *Chiaraluce et al.,* 2017; *Xu et al.,* 2017; *Scognamiglio et al.,* 2018; *Wang et al.,* 2018]. For lower fault dip angles (<35°) of segment F1 (Figures S5a-S5d), even if the LOS residuals in the Norcia area get lower (Figures S6a-S6f), the displacements (both horizontal and vertical) of all of the GPS stations in the footwall of the MVB fault system are badly reproduced, with a systematical underestimation of the footwall uplift (Figures S7a, S7b, S7e and S7f), and the modelled fault plane no longer passing through the hypocenter (Figure S5b and S5c). On the contrary, for higher fault dip angles (> 40°, Figures S5g-S5l), the residuals in the Norcia area and around the Rifugio Perugia hotel significantly increase (Figures S6j-S6r) and the footwall uplift is systematic overestimated (Figures S7n, S7r and S7v).

We then inverted the geodetic and SM-derived displacements assuming slip also on the large and blind antithetic fault (F2; 2-faults model, Figures 7e and 7f). For simplicity, we set the strike of the antithetic faults (F2 and F3) parallel to the main rupture (N339° striking), which is consistent with the distribution of aftershocks and surface geological evidence. The main antithetic fault (F2, Figure 7f) represents the blind steep (65° NE dipping) splay well illuminated by aftershock distribution (see also Figure 4 of *Cheloni et al.* [2017]) and that was likely partially activated during the M_W 5.4 aftershock occurred one hour after the 24 August Amatrice mainshock [*Scognamiglio et al.,* 2016]. The inclusion of segment F2 improves the fit to the geodetic data respect to the 1-fault model (yielding about 10-30% of RMS improvement for the different datasets; Table 1). Definitely, slip along this segment is necessary to fully explain the positive LOS displacement in the Norcia area (Figures 6d-6f and 6m-6o) and to improve the observed displacements at GPS stations RIFP and MSAN (Figures 5c and 5d). Removing this fault segment (1-fault model) significantly degrades the fit to the data and similarly to the results of *Walters et al.* [2018] in no way the Norcia lobe of deformation can be totally reproduced in both shape and amplitude (Figures 6a-6c and 6j-6l), even if we assume a very low (32°) and unreliable fault dip angle of segment F1 in the 1-fault model (Figures S6a-S6c).

Although the 2-faults model satisfactory reproduces the surface displacements, we still note significant residuals in the InSAR ALOS-2 displacement just in correspondence of the Rifugio Perugia antithetic fault trace emerging near the GPS RIFP station (Figures 6d-6f and 6m-6o). The addition of a third smaller dislocation corresponding to this antithetic fault (F3; 3-faults model, Figures 7i-7o) further reduces the RMS of each datasets (yielding about 7-17% of RMS improvement; Table 1), allowing us to better explain the observed GPS and LOS displacements also in this sector of the Castelluccio plain (Figures 5e-5h, 6g-6i and 6p-6r). The smaller antithetic segment (F3, Figure 7k) corresponds to the Rifugio Perugia antithetic fault (65° NE dipping) along which we found evidence of surface ruptures and minor shear planes that likely intersect to the south the damaged San Benedetto tunnel (Figures 2, 4e and 4f). In fact, it is interesting to note that the southern edge of the additional slip recovered on segments F2 and F3 well correlates with the observed surface fractures and with the damage zone of the concrete San Benedetto tunnel.

Finally, we constructed also a complex 6-faults model (Figures S8a-S8c) that includes all the faults from the previous best-fit 3-faults model as well as other smaller synthetic and antithetic splays that are evident in the aftershocks distribution (in particular, another antithetic fault is well evident near the 26 October Visso mainshock hypocenter; see Figure 3 of *Chiaraluce et al.* [2017]) and another one in the field (i.e., the Piano Perduto antithetic fault and the synthetic splay at the piedmont of Mt. Vettore). This model was constructed to evaluate the possible contribution of also these smaller structures to the overall deformation field. However, our results suggest that including or not these further dislocations in our best-fit 3-faults half-graben model do not affect the fit to the data (Figures S8d-S8h and Table 1). Indeed, their proximity to the main fault plane and/or their small scale make it difficult to tell and/or to solve possible additional slip also along these structures from our geodetic data and inversion scheme, in agreement with the results of *Walters et al.* [2018]. Another possibility is that the smaller structures in the proximity of the main fault trace are located in areas where the InSAR interferograms are incoherent and therefore they would be difficult to estimate.

Ultimately, we find that the geodetic data are well described (Figures 5 and 6) using a fault model with at least three fault segments (3-faults model, Figures 7i-7o), that yields 33%, 21%, 41%, 16% and 28% improvement in the RMS to the regional GPS, the near-field survey-mode GPS, the SM-derived displacements, the ALOS-2 and the SENT-1 data, respectively, when compared to the 1-fault model (Table 1). In all tested cases, some persistent residuals (up to ~20 cm) in the ALOS-2 displacements still remain along the fault trace of our preferred solution (Figures 6c, 6f and 6i). Some of these residuals correspond to known areas of incoherence in the ALOS-2 dataset, while others may suggest local complexities possibly associated with minor shallow strike variations of the main fault and/or to secondary structural complexities in the uppermost portions of the fault system and/or to the effect of topography not resolvable by means of elastic modelling in our simulations.

4.2 Complex Fault Arrangement Rupture Scenarios

Although the observed surface deformation is well reproduced (Figures 5e-5f, 6g-6i and 6p-6r) by our half-graben model (3-faults model, Figures 7i-7o), we tested also the possibility that a NE-SW striking and NW dipping structure, oblique to the main MVB fault system might have slipped during the 30 October earthquake, as proposed by *Scognamiglio et al.* [2018] and *Walters et al.* [2018]. Since the geometry and coseismic activation of inherited oblique structures in the rupture process of the 30 October earthquake are debated, in this section we explore a number of different geometries of the transverse structure (i.e., from low- to high-dip angle) and three different possible scenarios, that is, involving or not the antithetic segments.

(1) We first performed a number of joint inversions including in our preferred half-graben fault array a further and transverse ancillary dislocation (F4; 4-faults model; Figures 8, 9, 10, S9, S10 and S11), roughly corresponding to the hypothesized OAST ramp cross-structure. Similar to the study of *Scognamiglio et al.* [2018], we set therefore the strike of F4 segment (~N210°) parallel to the mean mapped trace of the OAST [e.g., *Cosentino et al.*, 2010; *Calamita et al.*, 2011; *Di Domenica et al.*, 2012; *Pierantoni et al.*, 2013], while varying its fault dip angle (between 20° and 70° in steps of 10°) to investigate how this might affect our results (Figures S9, S10 and S11). For low-angle solutions (F4 fault dip angles 20°, 30° and 40°) we resolve some normal slip (up to ~70-100 cm) also along this fault segment (F4) just beneath the Norcia deformation lobe and behind the antithetic faults (Figures S9a-S9l), which in turn accommodate a slightly smaller amount of slip than the 3-faults model (there is a trade-off between slip distribution on segments F2-F3 and segment F4 for low-angle solutions). For high-angle solutions (F4 fault dip values 50°, 60° and 70°), the retrieved normal slip is placed further to the southeast (Figures S9m-S9z). In all cases, including the segment F4 in the inversion does not contribute to improve the fit to the data (Tables 1 and 2 and Figures 8e, 8f, 9g-9i, 9p-9r, S10 and S11), while the retrieved slip distribution on segments F1, F2 and F3 is similar (Figures 10i-10o and S9).

(2) Another possibility consists in assuming slip along the main fault plane (F1), the blind antithetic fault (F2) and the cross-structure (F4), that is, not considering the contribution of the Rifugio Perugia antithetic fault (F3) to the total deformation field (Figures 8, 9, 10, S12, S13 and S14). As expected, the exclusion of segment F3 in the inversion causes slip on the oblique structure (F4) to slightly increase (up to ~80-110 cm, Figure S12) with respect to the previous 4-faults model (Figures 10i-l) and additional slip, characterized by a significant left-lateral strike-slip component, is resolved on segment F4 in correspondence of the smaller antithetic fault (Figures 10h). In all cases, we observe a slightly general improvement in the RMS of the data with respect to the 1-fault model (Tables 1 and 2), with values similar to the

2-faults (F1+F2) half-graben model but worse than our preferred 3-faults (F1+F2+F3) scenario. In addition, looking at the spatial variability in misfit, the deformation lobe in proximity of the Rifugio Perugia antithetic fault is never fully reproduced (Figures 9d-9f, 9m-9o and S13) and some residuals at GPS station RIFP still remain (Figures 8c, 8d and S14).

(3) Finally, one last possibility is to assume slip on the main normal fault plane (F1) and only on the cross-cutting structure (F4), that is, removing the coseismic contribution of both the F2 and F3 antithetic faults (Figures 10a-d and S15). This alternative model has been already tested by *Cheloni et al.* [2017] assuming a low fault dip angle of the transverse segment (fault dip 20°) and by *Scognamiglio et al.* [2018] assuming instead a fault dip angle of 36°. Modelling the ancillary segment F4 as a low-angle dislocation (fault dip angles 20° and 30°, Figures S15a-S15h) reduces the observed residuals (Figures S16a-S16f and S17a-S17h) with respect to the 1-fault model, but the segment F4 would cut the antithetic structures (Figure S15c, S15d, S15g and S15h; also see Figures 4h and 4j in *Cheloni et al.* [2017]). As in the previous case, the exclusion of a dislocation in the modelling (F2 segment) causes slip on the oblique structure (F4) to further increase (up to ~150 cm; Figure S15). In this case, the positive LOS deformation in the Norcia area is well reproduced only by imposing the end-member low-angle solution (fault dip angle 20°) of segment F4 (Figures S16a-S16c), while the GPS displacements at stations MSAN and the negative LOS deformation located in the Rifugio Perugia area remain not completely reproduced (Figures S16a-S16c and S17a-S17d), making the total RMS worse than both our preferred 2-faults and 3-faults half-graben models (Tables 1 and 2). In addition, such a flat geometry at depth of the OAST is not supported by any geological, seismological and geophysical evidence. Finally, we tested the hypothesis of a higher fault dip angle ($\geq$ 40°) of the segment F4. In this way the dislocation would get deeper than where we observed the major residuals (Figures S15i-S15z). Therefore, these models are not able to reproduce the observed complexities of the deformation field in the Norcia area and in the southern part of the Castelluccio plain (Figures S16g-S16r and S17i-S17z). Thus, by using a 2-faults model with the main (F1) fault and just the main (F2) antithetic fault the fit to the data is quite better than using a 2-faults model with the main fault and the oblique (F4) fault (RMS regional GPS 1.5 vs 1.6 cm; RMS survey-mode GPS 2.1 vs 2.8 cm; RMS SM-derived 1.2 vs 1.4 cm; RMS ALOS-2 4.0 vs 4.2 cm; RMS SENT-1 3.2 vs 3.5 cm, for the F1+F2 model and the F1+F4 model respectively).

In all of the tested scenarios, to include a low-to-moderately NW-dipping cross-cutting fault (F4) reduces the magnitude of retrieved slip in the deeper portion of the master F1 fault plane beneath the coseismic slip patch of the 24 August Amatrice event (see Figure 7i and 10i for comparison). There is indeed a trade-off between slip distribution on F1 and F4 segments, because the slip in the deeper portion of fault F1 spatially overlaps with the south-western part of the segment F4. In conclusion, although a rigorous statistical comparison between models is difficult due to variation in model parameters such as smoothing constraint and number of degrees of freedom, our analysis suggests that a primary coseismic activation of a cross-structures is not necessary to explain the observed surface displacement during the 30 October earthquake. In fact, it is only including the antithetic ancillary faults (which clearly were active in the sequence) in the modelling that the observed coseismic deformation is fully reproduced. We therefore believe that our preferred 3-faults half-graben dislocation model is justified because not only it reduces the residuals, but it has ground on independent geological and seismological observations, that is also honoring independent geological observations of ground ruptures and aftershocks distribution.

4.3 Testing more Complex Geometries of the MVB Master Fault

In this section we explore two different complex geometries of the master MVB fault, that is, testing the possibility that the actual geometry of the master fault is curved along strike or if the fault is listric down-dip. We therefore performed a number of inversions varying the dip and the geometry of the MVB fault to investigate how this might affect our results, including the best-fit antithetic sources (F2 and F3) in the modelling.

Looking at the ALOS-2 InSAR data (Figure 6), it seems that the strike of the northern portion (the Visso segment) of the MVB fault is slightly different from its southern part. To simulate this change, similarly to *Walters et al.* [2018], in the first test we subdivided the master fault into two segments, the southern one oriented ~N170° and the northern one ~N160° (Figures S18 and S19). In the second test we varied the dip of the master fault, subdividing down-dip the fault into a section ~40° SW dipping and a deeper portion ~30° SW dipping (Figures S20 and S21), to simulate a listric fault geometry.

A comparison between the different tested geometries indicates that, although our best-fit 3-faults model in which the MVB fault is a single straight fault segment (Figure 11) produces a slightly better fit than the others (Figures 5, 6, S19 and S21), the effect of the changing fault strike or fault dip with depth does not significantly change the RMS of the data. The retrieved slip distributions (Figures S18 and S20) for the complex master fault geometries are similar to that computed by means of a simple planar rupture plane (Figure 11), showing maximum slip of ~3m in the central part of the fault plane, between 5-7 km depth and southwestward respect to the hypocenter of the 30 October mainshock.

The most significant change with respect to our best-fit 3 faults planar model is that the deeper patch of slip beneath the 24 August slip patch disappears in the case of a listric geometry of the master fault (compare Figures S20 and 11). At the same time, a smaller patch of slip is retrieved slightly more to the south-west, between 7-9 km depth and below the Norcia basin, along the deepest part of the listric modelled F1 fault. Remarkably, this is an area that soon after the occurrence of the 30 October earthquake was interested by a number of M>4 normal-faulting events with focal mechanisms characterized by the SW-dipping plane with a relatively low-angle (≤30°) [*Chiaraluce et al.,* 2017].

5 Discussions

5.1 Half-Graben Models

Our preferred best-fitting dislocation model consists in a main N159° striking and 38° SW dipping normal fault (F1), releasing a seismic moment M_0 of 10.4×10^{18} Nm (using 30 GPa rigidity), equivalent to a M_W 6.6 earthquake (Table 3). The fault location is similar to that found in previous inversions of geodetic [*Cheloni et al.,* 2017; *Xu et al.,* 2017; *Walters et al.,* 2018; *Wang et al.,* 2018] and seismological [*Chiaraluce et al.,* 2017; *Scognamiglio et al.,* 2018] data, with the fault plane emerging near the mapped fault splays affecting the Mt. Vettore and Mt. Bove southwestern flanks (Figures 11, 12 and 13). Master fault plane solutions placed further to the SW [*Liu et al.,* 2017; *Pizzi et al.,* 2017] are not fully able to reproduce the westward and subsidence motion along the main fault traces, as observed by the local GPS network. This implies that coseismic slip has occurred both along the piedmont fault splay (trenched by *Galadini & Galli* [2003]) and along the Cordone del Vettore splay, where significant surface faulting indeed took place. Our retrieved ~40° dip of the master fault is consistent with the previous geodetic estimates (in the range 39°-43°) of *Cheloni et al.* [2017], *Xu et al.* [2017] and *Walters et al.* [2018], and with the seismological results (using near-source strong-motion records) of *Pizzi et al.* [2017], but it is quite different from the seismological estimate of *Scognamiglio et al.* [2018], who assumed a higher fault dip angle of

47° to model seismograms and GPS data. Our solution is also different from the geodetic estimate of *Wang et al.* [2018] who, instead, constructed an along-strike variable fault model with a fault dip angle of 33.5°.

Our slip pattern on the main fault is similar to the previous geodetic and seismological solutions [*Cheloni et al.,* 2017; *Chiaraluce et al.,* 2017; *Liu et al.,* 2017; *Papadopoulos et al.,* 2017; *Xu et al.,* 2017; *Walters et al.,* 2018; *Wang et al.,* 2018] that are characterized by one main coseismic asperity (up to ~3 m slip), with continuous rupture located up-dip (between 3-9 km depth) relative to the hypocenter (Figures 11 and 12). Nonetheless, thanks to the introduction in the modelling of the ancillary antithetic faults – i.e., both the structure observed in the field, which underwent surface rupture, and the major blind one illuminated by seismicity – our newly obtained slip distribution appears narrower than in the previous geodetic solutions, by using a simplified fault model [*Cheloni et al.,* 2017; *Xu et al.,* 2017; *Wang et al.,* 2018]. This makes our retrieved 30 October main coseismic patch less overlapped with the northern patch of the 24 August Amatrice earthquake. Moreover, by crossing the obtained slip distribution of the 30 October earthquake with the geologically defined geometry of the MVB source [*Falcucci et al.,* 2016; 2018], it appears that after the previous 24 August Amatrice and 26 October Visso mainshocks there was a large portion of unruptured fault plane to still generate a M ~6.5 earthquake (ultimately occurred on 30 October).

Our slip pattern on the master fault is different from the findings of *Scognamiglio et al.* [2018], who proposed two main slip patches, with similar peak slip value (~3 m) occurred up-dip from the nucleation, but on two differently oriented fault planes, that is, one slip patch on the main normal fault and other slip patch on a second NE-SW striking fault plane. Comparing the two slip distributions (see Figure 4 of *Scognamiglio et al.* [2018] and Figure 12), it appears that the slip patch on the transverse fault plane of *Scognamiglio et al.* [2018] spatially corresponds well with the southeastern portion of our largest asperity on our modelled main normal fault, although they are characterized by different rake angles (i.e., *Scognamiglio et al.* [2018] retrieved a significant left-lateral strike-slip component with respect to our almost pure dip-slip direction on the main slip patch). In this respect, our geodetically estimated fault dip angle of the master fault (38°) is similar to the dip angle of the second cross-cutting NE-SW striking fault plane (36°) of *Scognamiglio et al.* [2018]. Therefore, we issue that by just assuming a lower fault dip angle for the main fault the contribution of the transverse plane would significantly decrease, reconciling our geodetic solution with the seismological one. This is what appears in the geodetic study of *Walters et al.* [2018] in which, thanks to the use of a moderately dipping (40° dip) main normal fault and of a great number of ancillary fault segments, the contribution of a cross-cutting NE-SW striking dislocation in the rupture process of the 30 October earthquake is significantly reduced with respect to the *Scognamiglio et al.* [2018]'s study. Within this light, it is worth noting that the preferred fault plane geometry of *Pizzi et al.* [2018], with the best waveform fit, is characterized by a fault dip angle of 40° (that is, similar to the geodetic estimates) and appears able to reproduce the strong-motion data without the contribution of any secondary dislocations on transverse faults.

In addition, we resolved some slip (up to ~1 m) also in the shallower sectors of the area that was already affected by the 26 October Visso earthquake rupture (Figures 11a and 12a), where field observations revealed surface faulting due to the 30 October earthquake along both fault splays that underwent surface offset during the 26 October event and along others that have not ruptured during this event.

Similarly, our slip distribution involves meter-scale slip all around the northern coseismic patch of the 24 August Amatrice earthquake, both in the shallower and in the deeper portion of the assumed fault plane (Figures 11a and 12a). Slip in the shallow portion of the assumed fault plane fits with the field observations, that testified the increase of surface faulting formerly caused by the 24 August event, i.e., from ~20 cm to ~1.5-2 m after the 30 October shock along the main fault splay (Cordone del Vettore splay). As far as the deeper portion of the retrieved slip, assuming a slightly listric geometry of the master F1 fault (shown in paragraph 4.3, Figure S20), the deeper patch of slip beneath the 24 August earthquake disappears and, at the same time, a smaller patch of slip is retrieved slightly south-westward, between 7-9 km depth, along the low gradient part (assumed fault dip angle 30°) of the modelled fault. Although the geodetic data does not allow us to distinguish between a straight fault and a listric fault model, remarkably, this is an area that was interested by a number of M>4 normal-faulting events with focal mechanisms characterized by NW-SE striking and low-angle (≤30°) SW-dipping nodal planes soon after the 30 October earthquake [*Chiaraluce et al.*, 2017]. This suggests that 1) the main fault plane geometry may have a little variation of dip angle with depth, and 2) the only nodal planes of the main shocks may not be fully representative of the average geometry of the actual fault zone, considering that the 47° fault dip retrieved by the best-fit time-domain moment tensor solution is at 5 km depth (http://cnt.rm.ingv.it/tdmt/event/8863681) which is not the hypocentral depth.

In terms of main rupture, our model indicates that, in agreement with previous geodetic and seismological studies [*Cheloni et al.*, 2017; *Chiaraluce et al.*, 2017; *Xu et al.*, 2017; *Scognamiglio et al.*, 2018; *Walters et al.* 2018; *Wang et al.*, 2018], but differently from *Pizzi et al.* [2017], the 30 October earthquake did not propagate more southward than the epicenter of the 24 August event, as it did not reach the Amatrice area (Figure S22). This fact fits the seismological [*Chiaraluce et al.*, 2017] and geological information [*Galadini & Galli*, 2003; *Pizzi & Galadini*, 2009] which trace towards the SE the MVB fault system and the related seismogenic source [*Falcucci et al.* 2016; 2018] as far as the trace of the OAST, differently from the Mt. Vettore-Mt. Bove seismogenic source model proposed by *Valentini et al.* [2018], who prolong the seismogenic source more to the south. The OAST structure, cross-cutting the normal fault systems, could thus represent a strong lateral heterogeneity for the rupture propagation and, therefore, may act as fault segment boundary [*Falcucci et al.*, 2018]. In this perspective, the Mt. Vettore-Mt. Bove fault probably originated as a branch of the Ancona-Anzio lithospheric fault which has been positively inverted during the Pliocene becoming the OAST front [*Falcucci et al.*, 2018].

As regards the modelled secondary antithetic faults, they released less slip than the master fault, in agreement with the theoretical fault slip distribution between different fault segments in a half-graben structure, as suggested by boundary element model estimates [*Bruhn & Schultz*, 1996]. In particular, we resolved ~90 cm slip (at 2-5 km depth) along the major, blind antithetic fault (F2, Figures 11b and 12b), which released a seismic moment of 1.0×10^{18} Nm, equivalent to M_W ~6.0, and ~80 cm slip along the Rifugio Perugia smaller antithetic fault (F3, Figures 11b and 12c), which released a seismic moment of 0.4×10^{18} Nm, equivalent to M_W 5.7 (Table 3). Although that the two modelled antithetic faults likely join at depth, and both rooting on the master fault, yet our results suggest that these structures have accommodated separately part of the coseismic deformation. In this respect, the ancillary antithetic source proposed by *Cheloni et al.* [2017] represents an "halfway" solution of our two modelled antithetic faults, and our F2 segment is similar to the so-called Norcia antithetic fault in the study of *Walters et al.* [2018]. Differently, *Scognamiglio et al.* [2018] cannot fit the strong-motion and GPS data with only an antithetic structure (and the main fault of

course). However, the geometry of both the main fault and of the antithetic fault adopted by the authors appears quite different from our optimized best-fit model and from the *Walters et al.* [2018]'s model, which are instead able to reproduce the deformation field. Finally, a reconstruction of the subsurface geology of the area [*Porreca et al.*, 2018] based on a geological interpretation of unpublished seismic reflection profiles suggests the presence below the Castelluccio basin of a conjugate system of antithetic normal faults.

The total seismic moment released by our 3-faults model is 11.7×10^{18} Nm (Table 1), greater than seismic-only based estimates (e.g., 8.8×10^{18} Nm in *Scognamiglio et al.* [2018], combining the two faults). This discrepancy may be due to some aseismic slip along the whole fault network that was not captured by the seismic data and, therefore, that cannot be estimated by only seismic inversion. Indeed, even our 1-fault model already produces a geodetic moment greater than the seismological one. This could imply that a minor part of the whole retrieved slip on the activated fault array is either slow (or aseismic) or post-seismic.

In terms of fault rupture complexity, the contribution to the dislocation model of the antithetic faults completely accounts for those near- and far-field peculiar deformation features. In particular, we have demonstrated that 1) resolved slip on the largest, blind antithetic fault (F2) fully accounts for the uplift and westward shift of the Norcia area (Figures 6d-6f and 6m-6o); 2) the slip along the Rifugio Perugia antithetic fault (F3) is necessary to fit the local InSAR deformation lobe at the southern end of the rupture (surface faulting has been observed only along ~NW-SE striking fault planes; Figures 6g-6i and 6p-6r), as well as the dislocation of the San Benedetto tunnel; 3) although the Piano Perduto antithetic fault is probably too close to the main fault trace to be singularly told by our model (Figure S8c), the evidence of surface faulting along it (Figure 4d) indicates that also this secondary structure accommodated a non-negligible amount of coseismic slip up to the surface; 4) no significant additional coseismic slip on inherited cross-structures is required to reproduce the observed surface displacement during the 30 October earthquake. This point is extensively analyzed in the following.

5.2 Are Complex Fault Arrangement Models Really Necessary?

The evidence and considerations exposed below allow us to discard the hypothesis of a primary active role of the supposed cross-cutting NE-SW striking and NW dipping fault plane [*Cheloni et al.*, 2017; *Scognamiglio et al.*, 2018; *Walters et al.*, 2018] in the seismogenic process of the 30 October event:

- a low-angle transverse structure would cross-cut the observed high-angle antithetic faults (Figure S15);
- a high-angle transverse dislocation does not contribute to improve the fit to the data (Figures S9-S11);
- sections on the relocated seismicity made across the supposed oblique structure (see Figure 3 of *Chiaraluce et al.* [2017]) should have shown sub-horizontal clusters of aftershocks at increasing depths going from the OAST trace towards NW, i.e., supposedly enlightening the oblique structure; instead, these sections do not show any clear evidence of this;
- depending on its actual down-dip dimension and fault dip angle, an oblique dislocation would also cut the Norcia normal fault system, located some 10 km west of the MVB fault system, and which represents another major seismogenic structure of the central Apennines [*Galli et al.*, 2005];
- as no geological and geophysical information on the geometry, on the extent at depth, on the dip and strike angle of this supposed cross-structure are available, the deep geometry of the

OAST cannot be extrapolated by only considering its surface geometric characteristics (that is, by simply prolonging downward the low-angle plane at the surface);
- we did not find any long-term geological and morphotectonic evidence of the presence of an oblique fault in the southern part of the Castelluccio plain, nor evidence of surface rupture associated to it has been surveyed [*Galadini et al.,* 2017; *Civico et al.,* 2018; *Gori et al.,* 2018; *Villani et al.,* 2018]. Even if transverse high-angle synthetic normal faults which would connect at depth to the supposed low-angle transverse fault have been hypothesized [*Scognamiglio et al.,* 2018; *Walters et al.,* 2018], no evidence of these are present in the field, and they are not necessary to reconcile the geological setting of the southern portion of the Castelluccio plain (Figure 2, geological cross-sections, and Figure S2f). In addition, a recent study of *Villani et al.* [2018] suggests the presence of NE-SW trending faults in the southern part of the Castelluccio plain, but they related them to an earlier phase of the Castelluccio plain formation and that are not currently active; this adds doubts on the hypothesis made by other authors [e.g., *Coltorti & Farabollini, 1991; Scognamiglio et al.,* 2018; *Walters et al.,* 2018] about the importance of NE-SW striking faults located on the southern rim of the Castelluccio plain in leading the recent tectonics and seismotectonics of MVB fault system, and hence in the 30 October seismotectonic process;
- our inversion results and, as a matter of fact, the forward modelling of InSAR measurements by *Scognamiglio et al.* [2018] indicate that the complex deformation pattern observed in the southern part of the Castelluccio plain cannot be fully reproduced by the only introduction of a transverse structure. In details, their composite model – made of a steep (47°) main normal fault and a gently (36°) dipping transverse fault – while is able to well fit the strong-motion and GPS data, it is actually not able to fully reproduce the observed ascending and descending LOS deformation fields, indeed producing very high residuals, up to ~50 cm, an underestimation of the Norcia deformation lobe and an overestimation of the observed LOS along almost the Castelluccio plain;
- the presence of a NE-SW trending and NW dipping fault bounding to the south-east the Castelluccio plain may be suggested by the pattern of a few fringes of the descending ALOS-2 interferogram (http://www.eorc.jaxa.jp/ALOS-2/en/img_up/dis_pal2_ita-eq_20160825.htm), which seem to bend abruptly from NW-SE to NE-SW trending. Nonetheless, this particular pattern doesn't appear in the ascending interferogram, on which the fringes in the same area show a more gently bending trend depicting the lobes of deformation caused by the main fault and by the dislocation of the Rifugio Perugia antithetic fault;
- *Walters et al.* [2018] introduced a transverse fault (that is, a moderately dipping fault) to model the southern sector of the deformation zone and their modelling based on geodetic data well fits a cross-cutting structure (in addition to the major antithetic structure). On the one hand, the contribution of this structure to the overall dislocation is of course lower than that proposed by *Scognamiglio et al.* [2018]; on the other hand, also the *Walters et al.*'s model appears somehow critical in this area even with the introduction of the transverse fault as 1) some slip along the master fault crosses the transverse structure and 2) the residuals that remain if this structure is not modelled would be simply accounted by the activation of the Rifugio Perugia antithetic fault.

Hence, on these grounds, the hypothesis of the presence and of the primary active role of a low-angle transverse structure in the seismogenic process of the 30 October earthquake is in our opinion weak and appears less plausible than the activation of the antithetic faults, which clearly were active in the sequence, are visible in the field, underwent surface faulting and the activation of which fully reproduces the observed coseismic deformation.

Other evidence would suggest instead the presence of a high-angle inherited transverse compressional structure, but further to the SE with respect to that hypothesized by the previously mentioned authors, located in between the MVB and the Laga Mts. As observed by *Michele et al.* [2016] and *Chiaraluce et al.* [2017], the aftershocks associated to both the 24 August and the 30 October earthquakes appear confined in two separated clusters by the OAST and the Gran Sasso thrust, from the surface down to up ~6 km depth, with almost no events in between these compressional structures. This would be consistent with an almost vertical dip of the thrusts.
Moreover, the tomographic inversion of *Chiarabba et al.* [2018] would also suggest a first order vertical discontinuity between the OAST trace and the Laga Mts. This discontinuity is in good agreement with the location of the inherited lithospheric high-angle Ancona Anzio Line. In this respect, the NNE-SSW striking ramp of the OAST could therefore represent the expression of this discontinuity that separates the MVB fault system from the Amatrice fault, hence separating the two patches ruptured during the 24 August Amatrice earthquake.
As for the interpretation proposed by *Chiarabba et al.* [2018], the trace of the OAST is not actually located north of the northern rupture patch of the 24 August Amatrice earthquake, as drawn by the authors. In fact, it appears that the geodetically estimated northern coseismic patch of the 24 August earthquake extends over about 10 km towards NW from the 24 August epicenter, then beyond the OAST trace. Moreover, the hypothesized thrust ramp does not separate the northern rupture of the 24 August Amatrice earthquake from the 30 October rupture because the second event ruptured also a part of the portion of the MVB fault system activated during the previous 24 August event. Hence, on this basis, the seismic sources of the northern rupture of the 24 August Amatrice earthquake and of the 30 October events appear not separated by any thrust ramp.

The OAST has been hypothesized by *Pizzi et al.* [2017] and *Cirella et al.* [2018] as a structural barrier that hindered propagation towards the northwest of the 24 August 2016 rupture on the MVB fault. The authors define the OAST ramp as the down-dip prolongation of the OAST trace. As they traced the structure, the 24 August 2016 Amatrice northern slip patch would have been confined not only laterally (towards the northwest) by the thrust plane but also underneath it – as shown in Figure 4a of *Pizzi et al.* [2017] and Figures 5a and 5b of *Cirella et al.* [2018]. Nonetheless, this mismatches with the fact that, according to the *Cirella et al.* [2018]'s model, the rupture propagated up to the surface, where 5 km-long surface faulting have been seen along the "Cordone del Vettore" splay [e.g., EMERGEO Working Group, 2016]. *Cirella et al.* [2018]'s model, indeed, describes fault rupture that splitted into two propagating fronts as it hit the supposed OAST structural barrier, with one rupture front going down-dip and one going up-dip, reaching unhindered the surface. Such a dual and contrasting behavior of the supposed OAST during the same earthquake seems at least odd and not discussed by the authors. More likely, in our opinion – and as already postulated by *Chiaraluce et al.* [2017] – northwestward rupture propagation of the Amatrice earthquake has been halted by a "barrier" following the definition given by *Page et al.* [2005], that is, a region that has a higher frictional strength (yield stress) than the surrounding fault, which can delay rupture and can induce rupture front curvature. In addition, as stated before, a low-angle transverse structure (fault dip of 32° in the *Cirella et al.* 'study) would cross-cut the observed high-angle antithetic faults which, instead, are clearly visible in *Cirella et al.'* Figure 5b. Again, the fact that 30 October earthquake increased the surface offset caused by the previous Amatrice event, indicates no structural separation between the sources of the 24 August northern coseismic slip patch and of the 30 October event.

Overall, even if we do not discard the presence of a high-angle fault-transverse structure, coinciding with the Ancona-Anzio lithospheric fault (Figure 13), our results indicate that its role in the seismogenic process may have been ultimately passive, as it has only halted the 30 October rupture southward, and it did not actively accommodate a significant amount of coseismic slip. Definitively, even if the MVB normal fault system can result from the extensional inversion of a tectonic structure inherited by preceding tectonic phases (and in this context, our estimated gently-dipping ~40° master fault plane would be in agreement with this hypothesis), as postulated by other authors [e.g., *Bonini et al.*, 2016; *Falcucci et al.*, 2018], our model indicates that what has occurred during the 2016-2017 central Italy seismic sequence fitted the Quaternary kinematic behavior and slip history, the geometrical characteristics (as for the extent of the whole structure) and the maximum expected magnitude from the fault activation defined in the past years [e.g., *Galadini & Galli*, 2003]. These lines of evidence represent therefore a validation of the geological methods on which grounds the MVB seismogenic source has been defined and separated from the other seismogenic normal fault strands aligned with it [*Falcucci et al.*, 2016].

6 Conclusions

The 30 October 2016 M_W 6.6 Mt. Vettore-Mt. Bove earthquake represents the largest Italian, and worldwide, normal faulting seismic event that has been observed with an unprecedented set of modern geodetic, seismological and geological data. We revisited the rupture geometry of the Mt. Vettore-Mt. Bove earthquake by performing a joint inversion of a new geodetic and seismological dataset, exploring the structures involved in the coseismic dislocation, and discussing on the feasibility of a "simple conceptual" half-graben dislocation model *versus* a more complex fault arrangement rupture scenario to reproduce the observed coseismic deformation.

Dislocation modelling, coupled with the geological observations on the synthetic and antithetic fault segments and splays of the MVB fault system activated during the 30 October event, allowed us to improve the knowledge of the rupture of the M_W 6.6 Mt. Vettore-Mt. Bove earthquake, enhancing the already published source models. Our results, based not only on the minimization of the model residuals but also on other independent evidence as the long-term geology (which represents the effect of many seismic cycles), revealed that, although when examined in detail the rupture is complicated, there is no need to suppose a complex fault arrangement rupture scenario by invoking the coseismic activation of oblique structures to explain the whole seismic sequence. Instead the general picture of the 2016-2017 central Italy seismic sequence on the MVB fault system can be imaged as relatively simple and can be explained as the result of the activation of a half-graben normal fault system, that simultaneously ruptured both the master MVB normal fault and a number of synthetic and antithetic faults, whose presence is testified by Quaternary geological observations, seismological and geodetic evidence and along which surface faulting took place. Thus, in wider terms, can complex multi-fault arrangement rupture scenarios, supposed only basing on the minimization of the residuals of mathematical models, be considered either as reliable as or even more reliable than simpler conceptual rupture models (in this case a half-graben model) based on diverse lines of evidence coherent with one another?

Acknowledgments

We would like to thank the Associate Editor, and the two reviewers Laura Gregory (University of Leeds) and Mong-Han Huang (JPL-Caltech) for their constructive suggestions, which helped to deeply improve the manuscript. We are very grateful to Richard Walters (Durham University) for providing us with the Sentinel-1 data. We thank Paolo Zimmaro (UCLA) for the SM-derived offsets and Giorgio De Guidi (University of

Catania) for the local GPS measurements. We also thank Fabrizio Galadini, Marco Moro and Michele Saroli for precious discussion. Most of the figures have been created using the Generic Mapping Tools (GMT) software [*Wessel and Smith, 1998*]. The regional GPS measurements are available at ftp://gpsfree.gm.ingv.it/amatrice2016/static/Cosismico_30Oct2016_GPS_GdL_V1.dat; the local GPS observations can be found in the study of *De Guidi et al.* [2017], while SM-derived displacements and SAR interferograms can be obtained by contacting the corresponding author (daniele.cheloni@ingv.it).

References

Anzidei, M., P. Baldi, A. Pesci, A. Esposito, A. Galvani, F. Loddo, A. Cristofoletti, A. Massucci, and S. Del Mese (2005), Geodetic deformation across the central Apennines from GPS data in the time span 1999-2003, *Ann. Geophys.*, *48*(2), 259-271.

Bonini, L., F.E. Maesano, R. Basili, P. Burrato, M.M.C. Carafa, U. Fracassi, V. Kastelic, G. Tarabusi, et al. (2016), Imaging the tectonic framework of the 24 August 2016, Amatrice (central Italy) earthquake sequence: new roles for old players?, *Ann. Geophys.*, *59*(5), doi:10.4401/ag-7229.

Bruhn, R.L., and R.A. Schultz (1996), Geometry and slip distribution in normal fault systems: Implications for mechanics and fault-related hazards, *J. Geophys. Res.*, *101*(B2), 3401-3412, doi:10.1029/95JB03253.

Calamita, F., S. Satolli, V. Scisciani, P. Esestime, and P. Pace (2011), Contrasting style of fault reactivation in curved orogenic belts: Examples from the Central Apennines (Italy), *Geol. Soc. Am. Bull, 123*(5-6), 1097-1111, doi:10.1130/B30276.1

Cello, G., S. Mazzoli, E. Tondi, and E. Turco (1997), Active tectonics in the Central Apennines and possible implications for seismic hazard analysis in peninsular Italy, *Tectonophysics, 272*, 43-68, doi:10.1016/S0040-1951(96)00275-2.

Cheloni, D., E. Serpelloni, R. Devoti, N. D'Agostino, G. Pietrantonio, F. Riguzzi, M. Anzidei, A. Avallone, et al. (2016a), GPS observations of coseismic deformation following the 2016, August 24, Mw 6 Amatrice earthquake (central Italy): Data, analysis and preliminary fault model, *Ann. Geophys*., 59(5), doi:10.4401/ag-7269.

Cheloni, D., R. Giuliani, N. D'Agostino, M. Mattone, M. Bonano, G. Fornaro, R. Lanari, D. Reale, and S. Atzori (2016b), New insights into fault activation and stress transfer between en echelon thrusts: The 2012 Emilia, Northern Italy, earthquake sequence, *J. Geophys. Res., 121*, doi:10.1002/2016JB012823.

Cheloni, D., V. De Novellis, M. Albano, A. Antonioli, M. Anzidei, S. Atzori, A. Avallone, C. Bignami, et al. (2017), Geodetic model of the 2016 Central Italy earthquake sequence inferred from InSAR and GPS data, *Geophys. Res. Lett.*, 44(13), 6778-6787, doi:10.1002/2017GL073580.

Chiarabba, C., P. De Gori, M. Cattaneo, D. Spallarossa, and M. Segou (2018), Faults geometry and the role of fluids in the 2016-2017 Central Italy seismic sequence, *Geophys. Res. Lett.*, doi:10.1029/2018GL077485.

Chiaraluce, L., R. Di Stefano, E. Tinti, L. Scognamiglio, M. Michele, E. Casarotti, M. Cattaneo, P. De Gori, et al. (2017), The 2016 Central Italy seismic sequence: A first look at the mainshocks, aftershocks and source models, *Seismol. Res. Lett., 88*(3), doi:10.1785/0220160221.

Cirella, A., G. Pezzo, and A. Piatanesi (2018), Rupture Kinematics and Structural – Rheological Control of the 2016 Mw 6.1 Amatrice (Central Italy) Earthquake from Joint Inversion of Seismic and Geodetic Data, *Geophys. Res. Lett.*, doi:10.1029/2018GL080894.

Civico, R., S. Pucci, F. Villani, L. Pizzimenti, P.M. De Martini, R. Nappi, and the Open EMERGEO Working Group (2018), Surface ruptures following the 30 October 2016 Mw 6.5 Norcia earthquake, central Italy, *Journal of Maps*, doi:10.1080/17445647.2018.1441756.

Cosentino D., P. Cipollari, P. Marsili, and D. Scrocca (2010), The geology of Italy, 2010. In: Beltrando M., Peccerillo A., Mattei M., Conticelli S., Doglioni C. (Eds.), *Journal of the Virtual Explorer, Electronic edition, 36*, paper 11, 1441-8142.

D'Agostino, N. (2014), Complete seismic release of tectonic strain and earthquake recurrence in the Apennines (Italy), *Geophys. Res. Lett., 41*, 1155-1162, doi:10.1002/2014GL059230.

De Guidi, G., A. Vecchio, F. Brighenti, R. Caputo, F. Carnemolla, A. Di Pietro, M. Lupo, M. Maggini, et al. (2017), Brief communication: Co-seismic displacement on 26 and 30 October 2016 (Mw = 5.9 and 6.5) – earthquakes in central Italy from the analysis of a local GNSS network, *Nat. Hazards Earth Syst. Sci., 17*, 1885-1892, doi:10.5194/nhess-17-1885-2017.

Devoti, R., N. D'Agostino, E. Serpelloni, G. Pietrantonio, F. Riguzzi, A. Avallone, A. Cavaliere, D. Cheloni, et al. (2017), A combined velocity field of the Mediterranean region, *Ann. Geophys.*, *60*(2), doi:10.4401/ag-7059.

Di Domenica, A., A. Turtù, S. Satolli, and F. Calamita (2012), Relationship between thrusts and normal faults in curved belts: new insight in the inversion tectonics of the Central-Northern Apennines (Italy), *J. Struct. Geol., 42*, 104-117, doi:10.1016/j.jsg.2012.06.008.

EMERGEO Working Group (2016), Coseismic effects of the 2016 Amatrice seismic sequence: First geological results, *Ann. Geophys., 59*(5), doi:10.4401/ag-7195.

Falcucci, E., S. Gori., F. Galadini, G. Fubelli, M. Moro, and M. Saroli (2016), Active faults in the epicentral area and mesoseismal Ml 6.0 24, 2016 Amatrice earthquake region, central Italy. Methodological and seismotectonics issues, *Ann. Geophys., 59*(5), doi:10.4401/ag-7266.

Falcucci, E., S. Gori, C. Bignami, G. Pietrantonio, D. Melini, M. Moro, M. Saroli, and F. Galadini (2018), The Campotosto seismic gap in between the 2009 and 2016-2017 seismic sequences of central Italy and the role of inherited lithospheric faults in regional seismotectonics settings, *Tectonics, 37*(8), doi:10.1029/2017TC004844.

Fletcher, J.M., M.E. Oskin, and O.J. Teran (2016), The role of a keystone fault in triggering the complex El Mayor-Cucapah earthquake rupture, *Nat. Geosci., 9,* doi:10.1038/NGEO2660.

Galadini, F., and P. Galli (2003), Paleoseismology of silent faults in the Central Apennines (Italy): the Mt. Vettore and Laga Mts. faults, *Ann. Geophys., 46*(5), 815-836, doi:10.4401/ag-3457.

Galadini, F., E. Falcucci, S. Gori, R.E. Kayen, B. Lingwall, A. Pizzi, A. Di Domenica, P. Zimmaro, and J.P. Stewart (2017), Chapter 2: Seismic source and surface rupture, in *Engineering Reconnaissance Following the 2016 central Italy earthquakes – Version 2,* edited by P. Zimmaro and J.P. Stewart, Geotechnical Extreme Events Reconnaissance Association Report No. GEER-050D, 33-50, doi:10.18118/G6HS39.

Galli, P., F. Galadini, and F. Calzoni (2005), Surface faulting in Norcia (central Italy): a "paleoseismological perspective", *Tectonophysics, 403*(1-4), 117-130, doi:10.1016/j.tecto.2005.04.003.

Galli, P., F. Galadini, and D. Pantosti (2008), Twenty years of paleoseismology in Italy, *Earth Sci. Rev., 88*(1-2), 89-117, doi:10.1016/j.earscirev.2008.01.001.

Galli, P., A. Galderisi, M. Martino, and G. Scarascia Mugnozza (2017), L'eccezionale caso della fagliazione della galleria San Benedetto il 30 Ottobre 2016, *GNGTS conference paper*, 37-41.

Galvani, A., M. Anzidei, R. Devoti, A. Esposito, G. Pietrantonio, A.R. Pisani, F. Riguzzi, amd E. Serpelloni (2012), The interseismic velocity field of the central Apennines from a dense GPS network, *Ann. Geophys., 55*(5), 1039-1049, doi:10.4401/ag-5634.

Gori, S., E. Falcucci, F. Galadini, P. Zimmaro, A. Pizzi, R.E. Kayen, B.N. Lingwall, M. Moro, M. Saroli, G. Fubelli, A. Di Domenica, J.P. Stewart (2018), Surface Faulting Caused by the 2016 Central Italy Seismic Sequence: Field Mapping and LiDAR/UAV Imaging, *EARTHQUAKE SPECTRA, 34*, 1585-1610, doi:10.1193/11141EQS236MR.

Hamling, I. J., *et al.* (2017), Complex multifault rupture during the 2016 M_W 7.8 Kaikoura earthquake, New Zealand, *Science, 356*(6334), doi:10.1126/science.aam7194.

Huang, M.-H., E.J. Fielding, C. Liang, P. Milillo, D. Bekaert, D. Dreger, and J. Salzer (2017), Coseismic deformation and triggered landslides of the 2016 Mw 6.2 Amatrice earthquake in Italy, *Geophys. Res. Lett., 44*, 1266-1274, doi:10.1002/2016GL071687.

INGV Working Group "GPS Geodesy" (2016), Preliminary co-seismic displacements for the October 26 (Mw5.9) and the October 30 (Mw6.5) central Italy earthquakes from the analysis of GPS stations, doi:10.5281/zenodo.167959.

Lavecchia, G., R. Castaldo, R. de Nardis, V. De Novellis, F. Ferrarini, S. Pepe, F. Brozzetti, G. Solaro, et al. (2016), Ground deformation and source geometry of the 24 August 2016 Amatrice earthquake (Central Italy) investigated through analytical and numerical modeling of DInSAR measurements and structural-geological data, *Geophys. Res. Lett., 43*, 12,389-12,398, doi:10.1002/2016GL071723.

Liu, C., Y. Zheng, Z. Xie, and X. Xiong (2017), Ruptures features of the Mw 6.2 Norcia earthquake and its possible relationship with strong seismic hazards, *Geophys. Res. Lett., 44*,1320-1328, doi:10.1002/2016GL071958.

Michele, M., R. Di Stefano, L. Chiaraluce, M. Cattaneo, P. De Gori, G. Monachesi, D. Latorre, S. Marzorati, L. Valoroso, C. Ladina, et al. (2016), The Amatrice 2016 seismic sequence: A preliminary look at the mainshock and aftershocks distribution, *Ann. Geophys., 59*, doi:10.4401/ag-7227.

Okada, Y. (1985), Surface deformation due to shear and tensile faults in a half-space, *Bull. Seism. Soc. Am., 75*(4), 1135-1154.

Page, M.T., E.M. Dunham, and J.M. Carlson (2005), Distinguishing barriers and asperities in near-source ground motion, *J. Geophys. Res., 110*(B11), doi:10.1029/2005JB003736.

Papadopoulos, G.A., A. Ganas, A. Agalos, A. apageorgiou, I. Triantafyllou, Ch. Kontes, I. Papoutsis, and G. Diakogianni (2017), Earthquake Triggering Inferred from Rupture Histories, DInSAR Ground Deformation and Stress-Transfer Modelling: The Case of Central Italy During August 2016-January 2017, *Pure Appl. Geophys.*, 174, 3689-3711, doi:10.1007/s00024-017-1609-8.

Pierantoni, P., G. Deiana, and S. Galdenzi (2013), Stratigraphic and structural features of the Sibillini Mountains (Umbria-Marche Apennines, Italy), *Italian Journal of Geosciences, 132*(3), 497-520, doi:10.3301/IJH.2013.08.

Pizzi, A., and F. Galadini (2009), Pre-existing cross-structures and active fault segmentation in the northern-central Apennines (Italy), *Tectonophysics, 476*(1-2), doi:10.1016/j.tecto.2009.03.018.

Pizzi, A., A. Di Domenica, F. Gallovic, L. Luzi, and R. Puglia (2017), Fault Segmentation as Constraint to the Occurrence of the Main Shocks of the 2016 Central Italy Seismic Sequence, *Tectonics,* 36, doi:10.1002/2017TC004652.

Porreca, M., G. Minelli, M. Ercoli, A. Brobia, P. Mancinelli, F. Cruciani, C. Giorgetti, F. Carboni, F. Mirabella, G. Cavinato, A. Cannata, C. Pauselli, and M.R. Barchi (2018), Seismic reflection profiles and subsurface geology of the area interested by the 2016-2017 earthquake sequence (Central Italy), *Tectonics, 37*(4), doi:10.1002/2017TC004915.

Resor, P.G., D.D. Pollard, T.J. Wright, and G.C. Beroza (2005), Integrating high-precision aftershock locations and geodetic observations to model coseismic deformation associated with the 1995 Kozani-Grevena earthquake, Greece, *J. Geophys. Res., 110*(B09402), doi:10.1029/2004JB003263.

Scognamiglio, L., E. Tinti, and M. Quintiliani (2016), The first month of the 2016 Amatrice seismic sequence: Fast determination of time domain moment tensors and finite fault model analysis of the M_L 5.4 aftershock, *Ann. Geophys., 59*, doi:10.4401/ag-7246.

Scognamiglio, L., E. Tinti, E. Casarotti, S. Pucci, F. Villani, M. Cocco, F. Magnoni, A. Michelini, and D. Dreger (2018), Complex fault geometry and rupture dynamics of the Mw 6.5, 2016, October 30th central Italy earthquake, *J. Geophys. Res., 123*(4), doi:10.1002/2018JB015603.

Stark, P.B., and R.L. Parker (1995), Bounded-values least-squares algorithm – An algorithm and implications, *Comput. Stat., 10(2), 129-141.*

Tinti, E., A. Scognamiglio, A. Michelini, and M. Cocco (2016), Slip heterogeneity and directivity of the Ml 6.0, 2016, Amatrice earthquake estimated with rapid finite-fault inversion, *Geophys. Res. Lett., 43*, 10,745-10,752, doi:10.1002/2016GL071263.

Valentini, A., F. Visini, and B. Pace (2017), Integrating faults and past earthquakes into a probabilistic seismic hazard model for peninsular Italy, *Nat. Hazards Earth Syst. Sci.,17*, 2017-2039, https://doi.org/10.5194/nhess-17-2017-2017.

Valerio, E., P. Tizzani, E. Carminati, C. Doglioni, S. Pepe, P. Petricca, C. De Luca, C. Bignami, G. Solaro, R. Castaldo, V. De Novellis, and R. Lanari (2018), Ground Deformation and Source Geometry of the 30 October 2016 Mw 6.5 Norcia Earthquake (Central Italy) Investigated Through Seismological Data, DInSAR

Measurements, and Numerical Modelling, *Remote Sens.*, *10*, 1901, doi:10.3390/rs10121901.

Valoroso, L., L. Chiaraluce, D. Piccinini, R. Di Stefano, D. Schaff, and F. Waldhauser (2013), Radiography of a normal fault system by 64,000 high-precision earthquake locations: The 2009 L'Aquila (central Italy) case study, *J. Geophys. Res., 118*, doi:10.1002/jgrb.50130.

Villani, F., R. Civico, S. Pucci, L. Pizzimenti, R. Nappi., P.M. De Martini, and the Open EMERGEO Working Group (2018), A database of the post-30 October 2016 Norcia earthquake coseismic effects in Central Italy, *Scientific Data*, doi:10.1038/sdata.2018.49.

Villani, F., V. Sapia, P. Baccheschi, R. Civico, G. Di Giulio, M. Vassallo, M. Marchetti, and D. Pantosti (2018), Geometry and structure of a fault-bounded extensional basin by integrating geophysical surveys and seismic anisotropy across the 30 October 2016 Mw 6.5 earthquake fault (central Italy): the Pian Grande di Castelluccio basin, *Tectonics*, doi:10.1029/2018TC005205.

Walters, R.J., L.C. Gregory, L.N.J. Wedmore, T.J Craig, K. McCaffrey, M. Wilkinson, J. Chen, Z. Li, J.R. Elliott, H. Goodall, F. Iezzi, F. Livio, A.M. Michetti, G. Roberts, and E. Vittori (2018), Dual control of fault interactions on stop-start rupture in the 2016 Central Italy seismic sequence, *Earth Planet. Sci. Lett., 500*, doi:10.1016/j.epsl.2018.07.043.

Wang, W., W. Sun, and Z. Jiang (2010), Comparison of fault models of the 2008 Wenchuan earthquake (Ms8.0) and spatial distributions of co-seismic deformations, *Tectonophysics, 491*, doi:10.1016/j.tecto.2009.08.035.

Wang, L., H. Gao, G. Feng, and W. Xu (2018), Source parameters and triggering links of the earthquake sequence in central Italy from 2009 to 2016 analyzed with GPS and InSAR data, *Tectonophysics, 774*, 285-295, doi:10.1016/j.tecto.2018.07.013.

Wessel, P., and W.H.F. Smith (1998), New improved version of the generic mapping tools released, *Eos. Trans. AGU*, *79*(47), 579-579, doi:10.1029/98EO00426.

Wilkinson, M.W., K.J.W. McCaffrey, R.R. Jones, G.P. Roberts, R.E. Holdsworth, L.C. Gregory, R.J. Walters, L. Wedmore, et al. (2017), Near-field fault slip of the 2016 Vettore Mw 6.6 earthquake (Central Italy) measured using low-cost GNSS, *Scientific Reports, 7*(4612) doi:10.1038/s41598-017-04917-w.

Xu, G., C. Xu, Y. Wen, and G. Jiang (2017), Source Parameters of the 2016-2017 Central Italy Earthquake Sequence from the Sentinel-1, ALOS-2 and GPS data, *Remote Sens., 9*, 1182, doi:10.3390/rs9111182.

Zimmaro, P., G. Scasserra, J.P. Stewart, T. Kishida, G. Tropeano, M. Castiglia, and P. Pelekis (2018), Strong motion characteristics from 2016 Central Italy earthquake sequence, *EARTHQUAKE SPECTRA*, doi:10.1193/091817EQS184M.

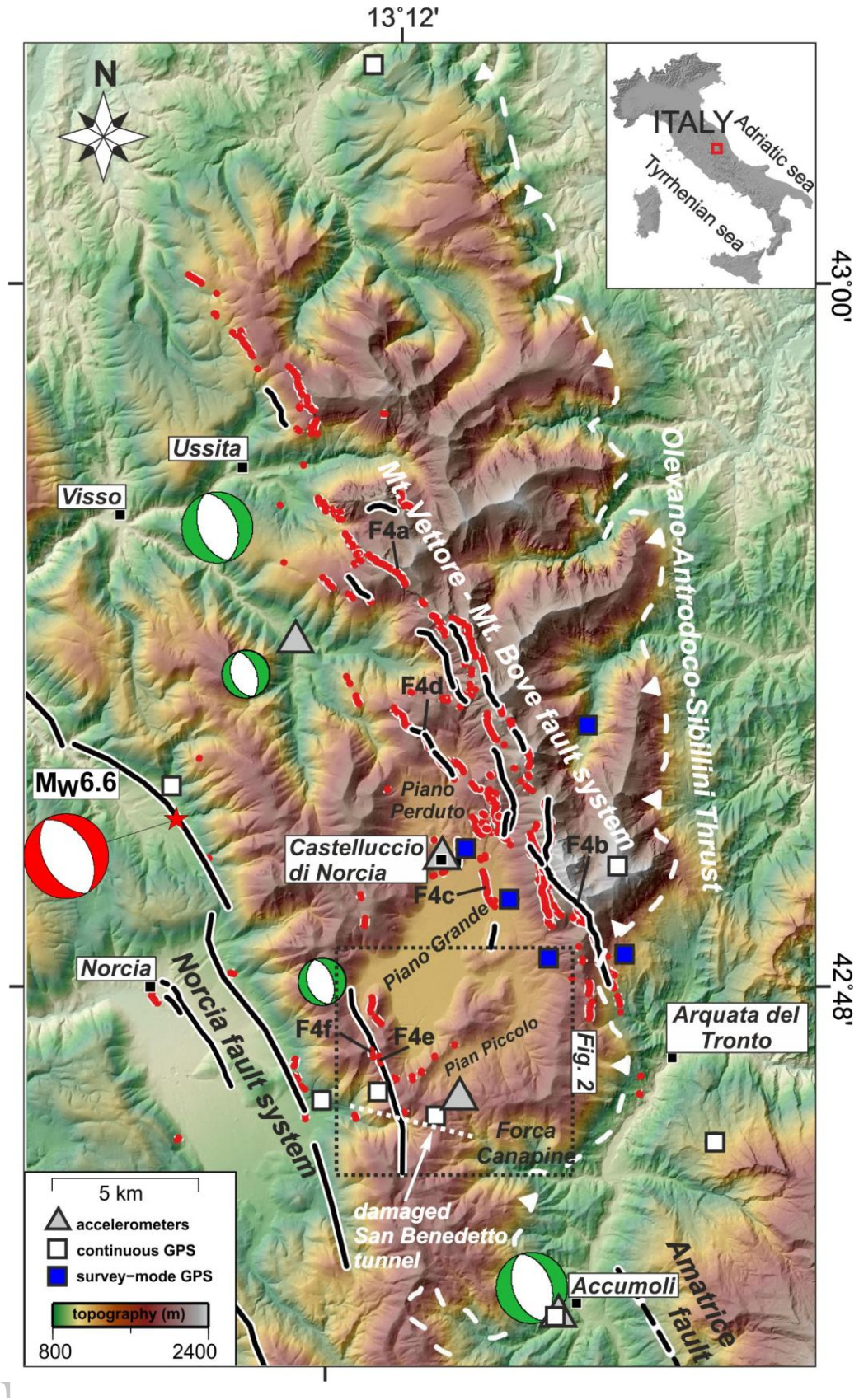

Figure 1. Seismotectonic settings of the 2016 epicentral area in central Italy. The black lines represent the major mapped active normal fault systems with associated splays [*Falcucci et al.*, 2016]. The white dashed barbed lines are older inherited thrusts [*Pizzi & Galadini*, 2009]. The red lines are surface ruptures along the ~28 km long MVB fault system and along the

antithetic and synthetic splays [*Civico et al.* 2018]. The red star indicates the 30 October M_W 6.6 epicenter. Beach-balls represent M_W>5 regional moment tensor solution available at http://www.cnt.rm.ingv.it/tdmt: from south to north, the 24 August Mw 6.2 Amatrice event; the 24 August Mw 5.4 shock, and the 26 October Mw 5.4 and 5.9 Visso events). The white arrow indicates the damaged zone of the concreted San Benedetto tunnel (white dashed line). Squares and triangles represent the location of the geodetic and seismic stations, respectively.

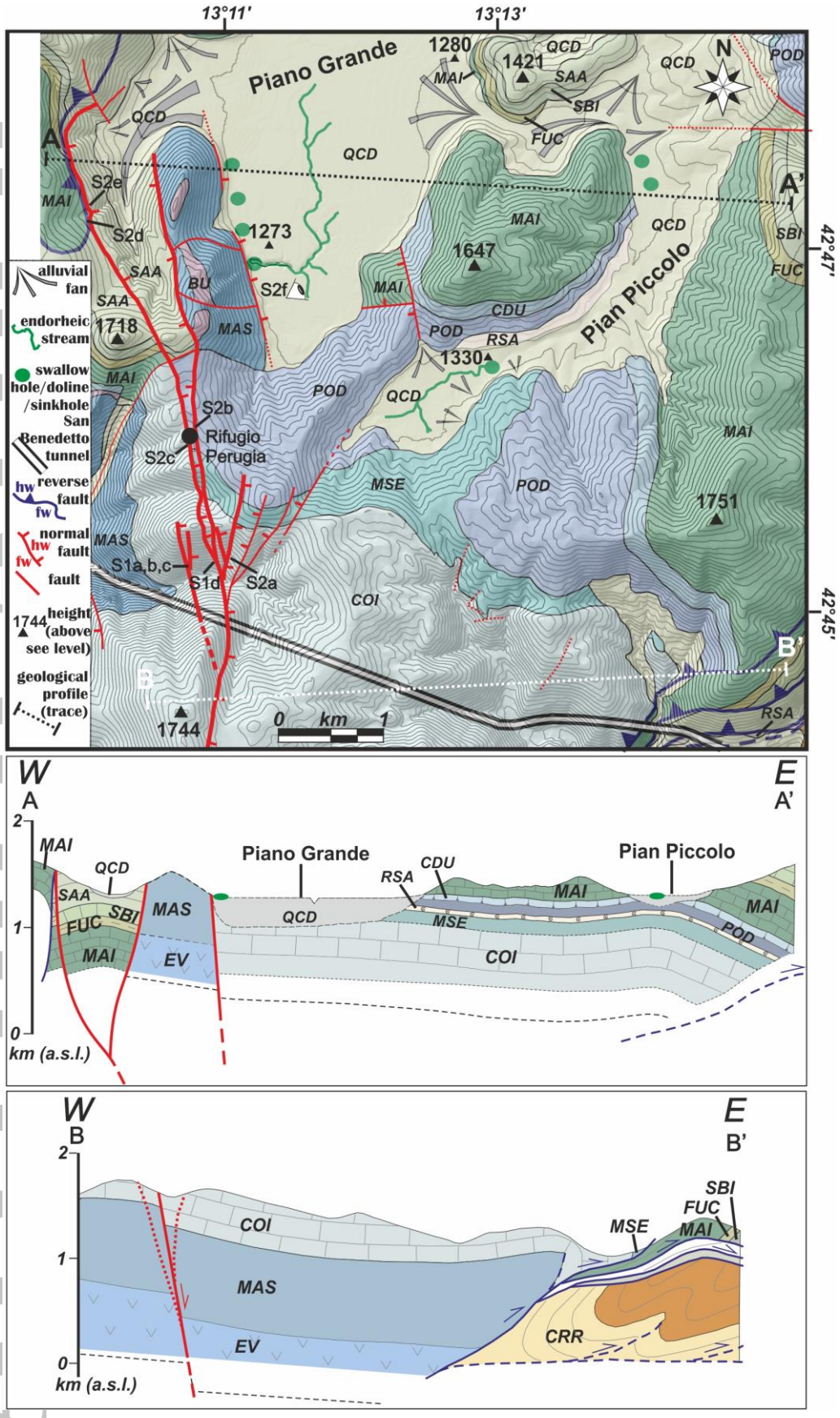

Figure 2. Geological map of the south-western border of the Castelluccio plain (redrawn and modified from *Pierantoni et al.* [2013]). Meso-Cenozoic marine carbonate bedrock

formations: SAA, Scaglia Rossa; SBI Scaglia Bianca; FUC, Marne a Fucoidi; MAI, Maiolica; CDU, Calcari diasprigni; POD, Calcari a Posidonia; RSA, Rosso ammonitico; MSE, Marne del Serrone; COI, Corniola; BU, Bugarone Group; MAS, Calcare massiccio; EV, Evaporiti. QCD, Quaternary continental deposits (slope, alluvial and lacustrine deposits). Red lines are normal faults. Thick red lines mark the antithetic faults investigated in the present study. Geological section B-B' is redrawn and modified from section F of *Pierantoni et al.* [2013].

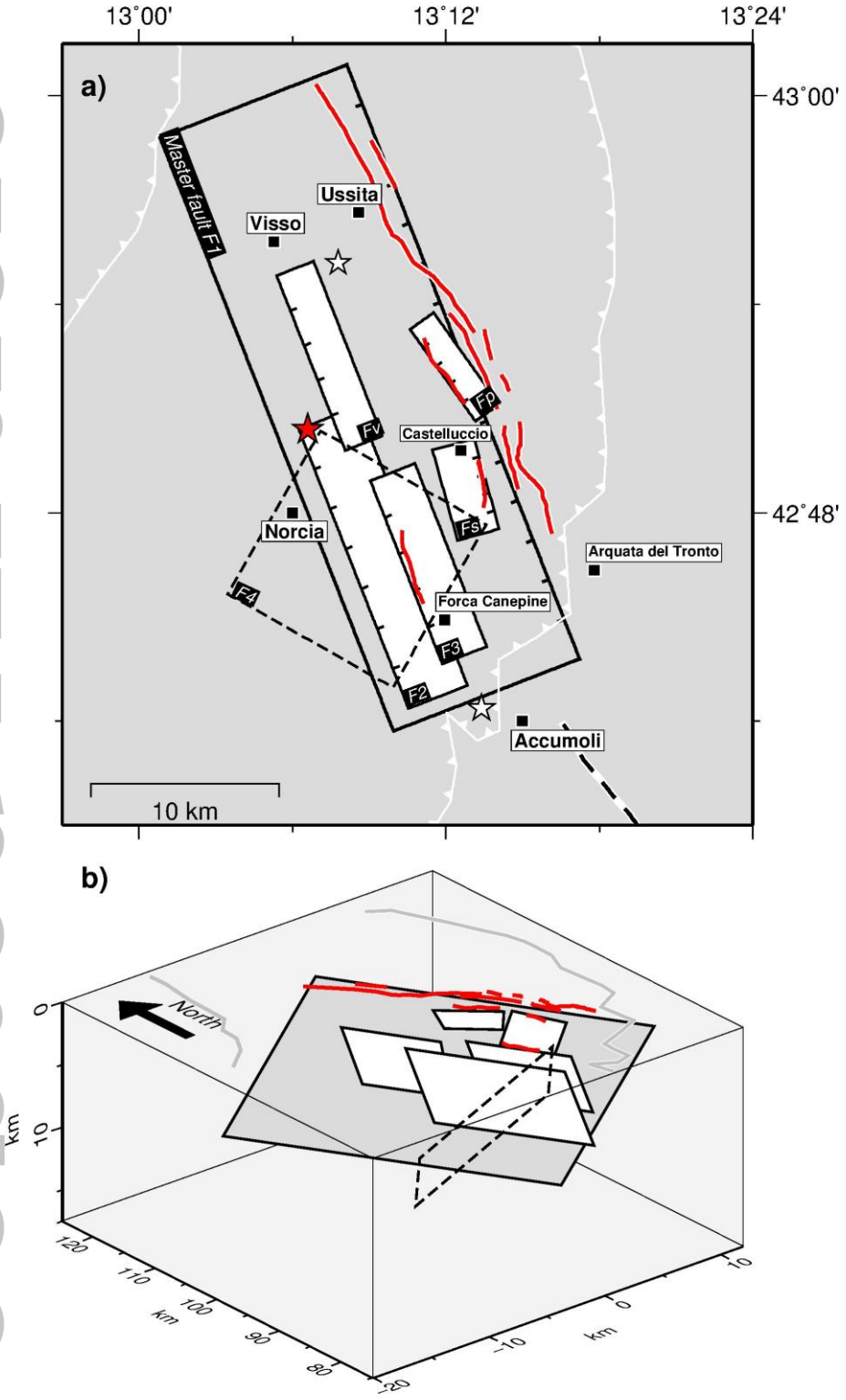

Figure 3. Interpreted fault network. (a) Map view. (b) Three-dimensional oblique view from south-west. Red lines on upper surface are simplified trace of the active MVB normal fault system with associated splays (modified from *Falcucci et al.* [2016]), while gray lines are the trace of the inherited thrusts (in white in map view). Other symbols as in Figure 1. Legend: F1, master MVB normal fault; F2, main blind antithetic fault; F3 Rifugio Perugia antithetic fault; Fv, antithetic splay located near the Visso mainshock; Fp, Piano Perduto antithetic fault; Fs, hanging-wall synthetic splay; F4 oblique NW-dipping dislocation.

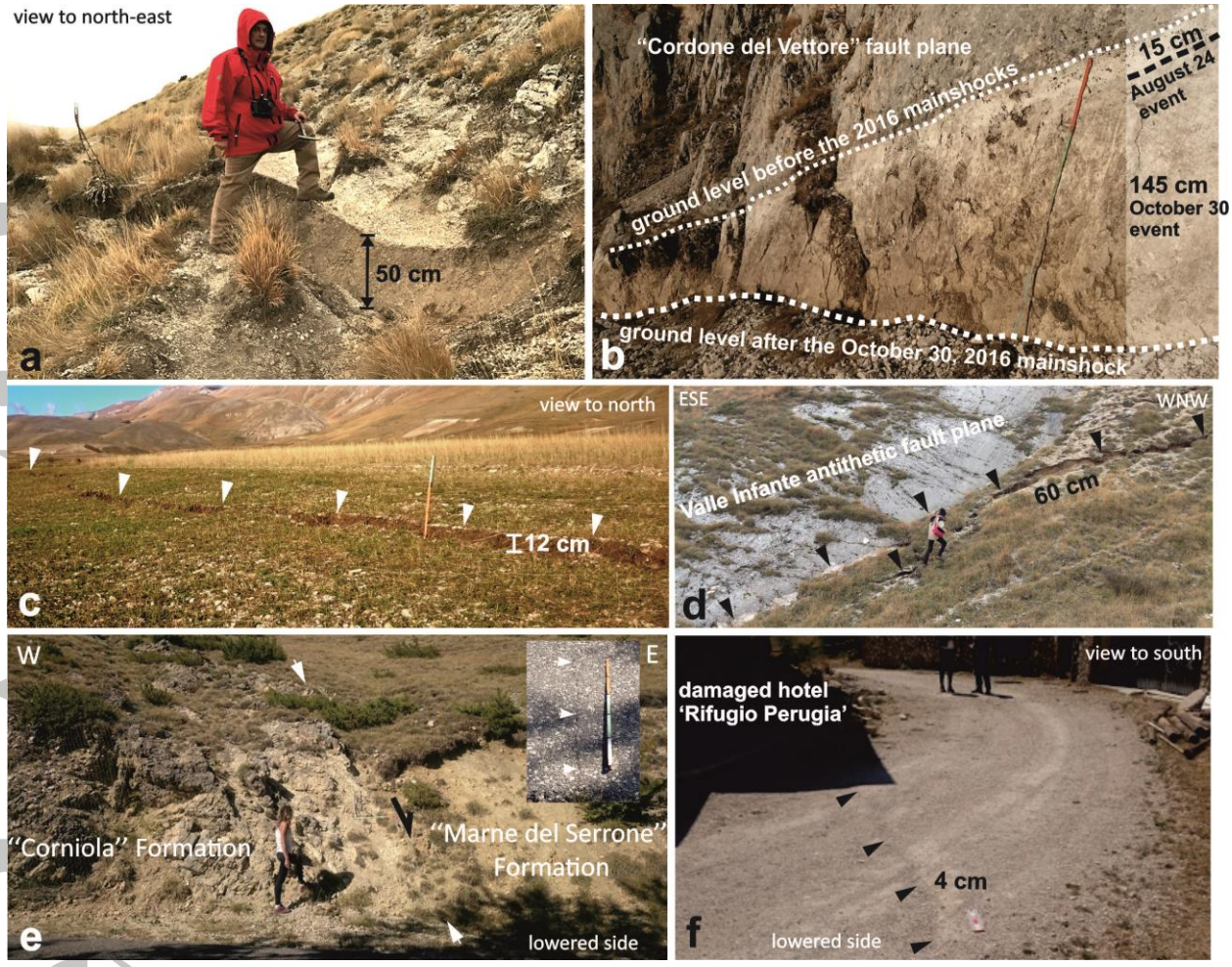

Figure 4. Surface ruptures after the 30 October event mapped in our study. (a) Mt. Bove fault segment (location at 42°54'50'', 13°11'29''; (b) Cordone del Vettore fault scarp (location at 42°49'3'', 13°15'13''; (c) synthetic fault splay located in the piedmont area of Mt. Vettore (location at 42°49'4'', 13°13'23''); (d) the Valle Infante antithetic fault (location at 42°51'58'', 13°12'1''); (e) the Rifugio Perugia antithetic fault (location at 42°45'42'', 13°10'51'') (inset: ground fractures along the road); (f) ground cracks near the Rifugio Perugia hotel aligned along the antithetic fault (location at 42°45'59'', 13°10'45'').

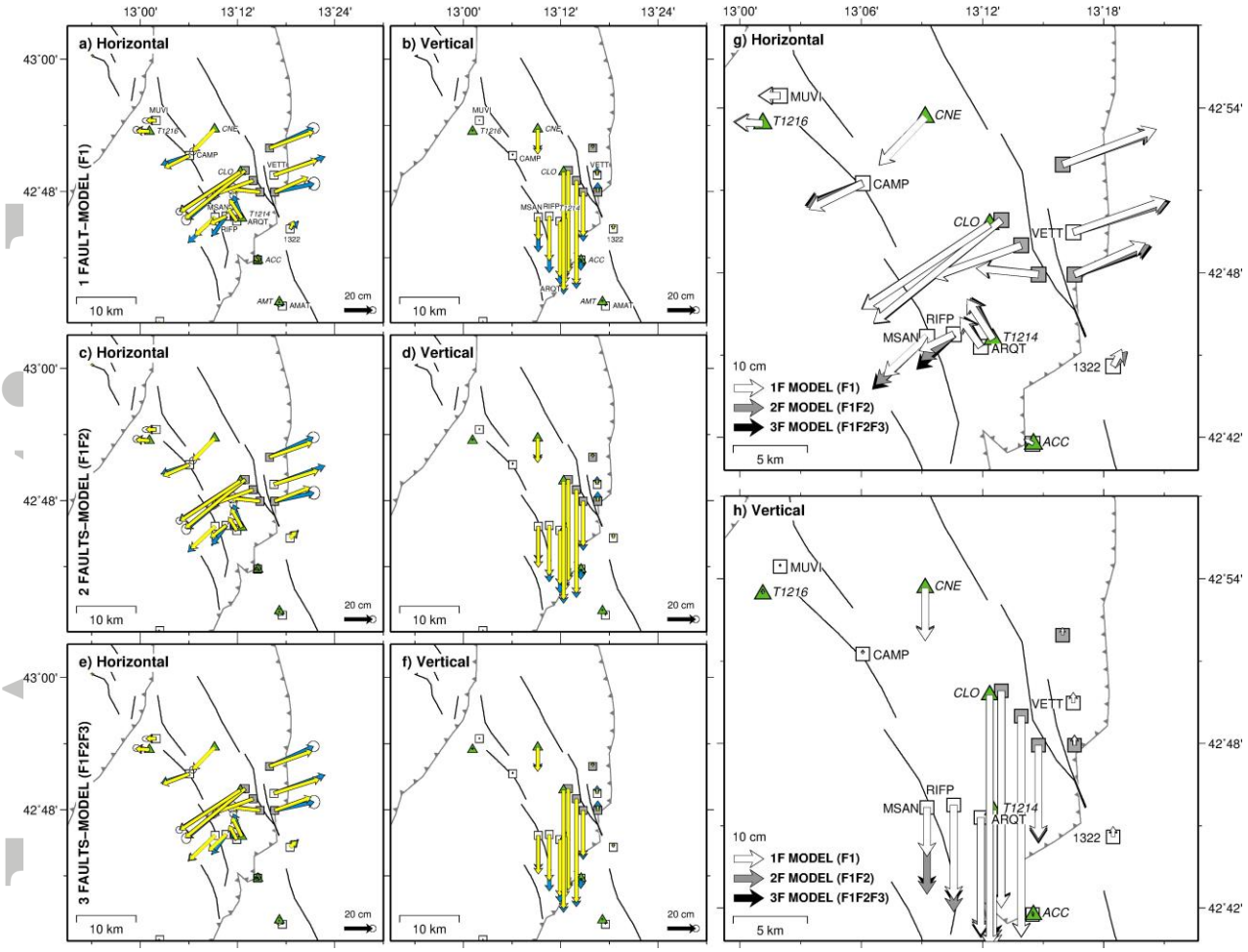

Figure 5. Observed and modelled GPS and SM-derived coseismic offsets based on the half-graben rupture scenarios. Panels a-b, 1-fault model (F1); panels c-d, 2-faults model (F1+F2); panels e-f, 3-faults model (F1+F2+F3). Observed (blue) and predicted (yellow) regional (white rectangles) and survey-mode (blue rectangles) GPS and SM-derived (triangles) horizontal and vertical displacements. Panels g-h show the synthetic offsets from all of the different models (the displacements are shown by gray-scale vectors; white for displacement based on 1-fault model through to black for displacement based on 3-faults model). Other symbols as in Figure 1.

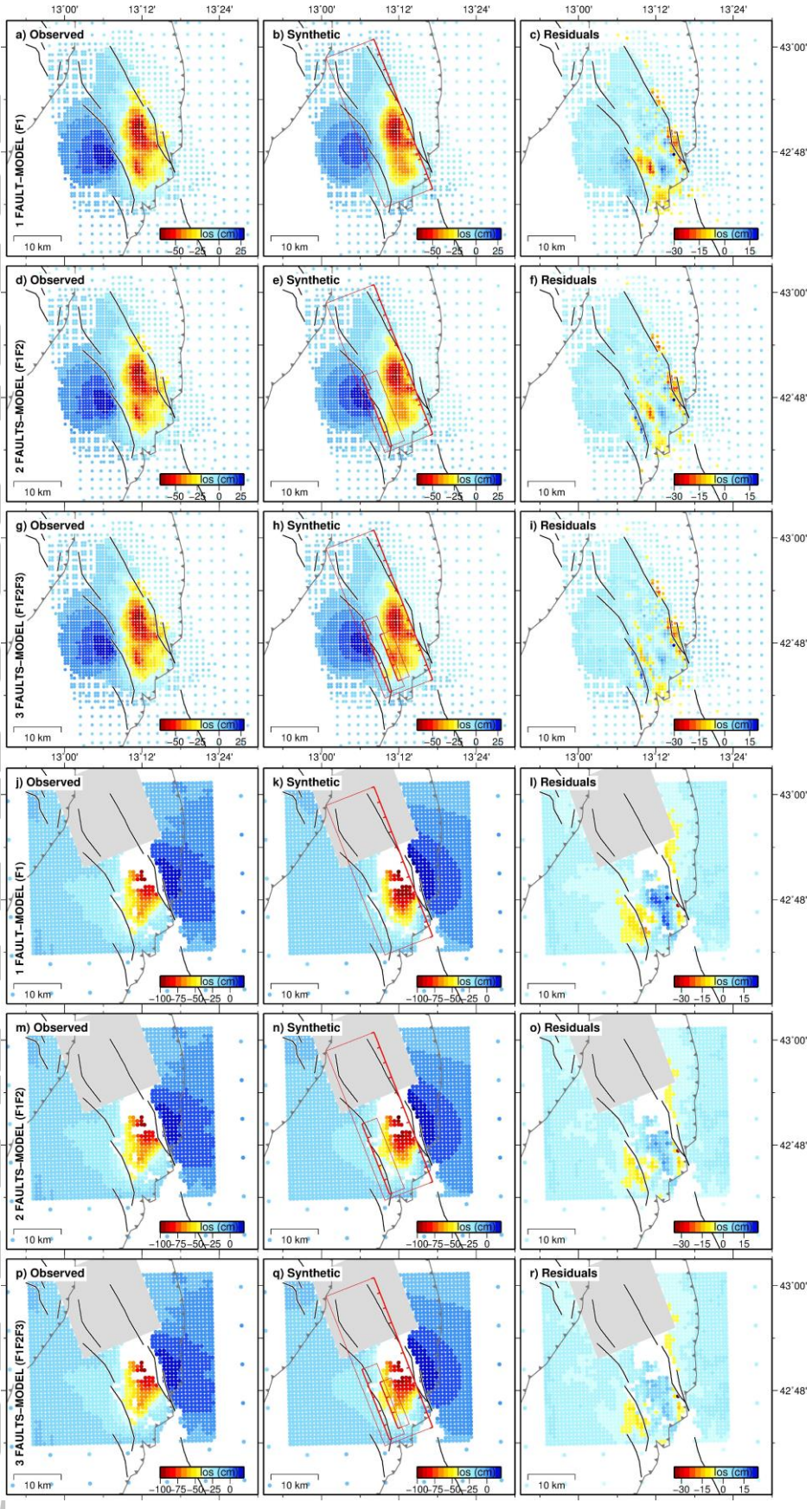

Figure 6. Observed, modelled and residual InSAR ALOS-2 ascending and SENT-1 descending unwrapped interferograms based on the half-graben rupture scenarios. Panels a-c

and j-l, 1-fault model (F1); panels e-f and m-o, 2-faults model (F1+F2); panels g-i and p-r, 3-faults model (F1+F2+F3). The red boxes indicate the fault segments modelled to have slipped during the earthquake in the different scenarios. The gray area shows the cut of the northern part of the SENT-1 descending interferogram, that was affected by the 26 October Visso earthquake. Other symbols as in Figure 1.

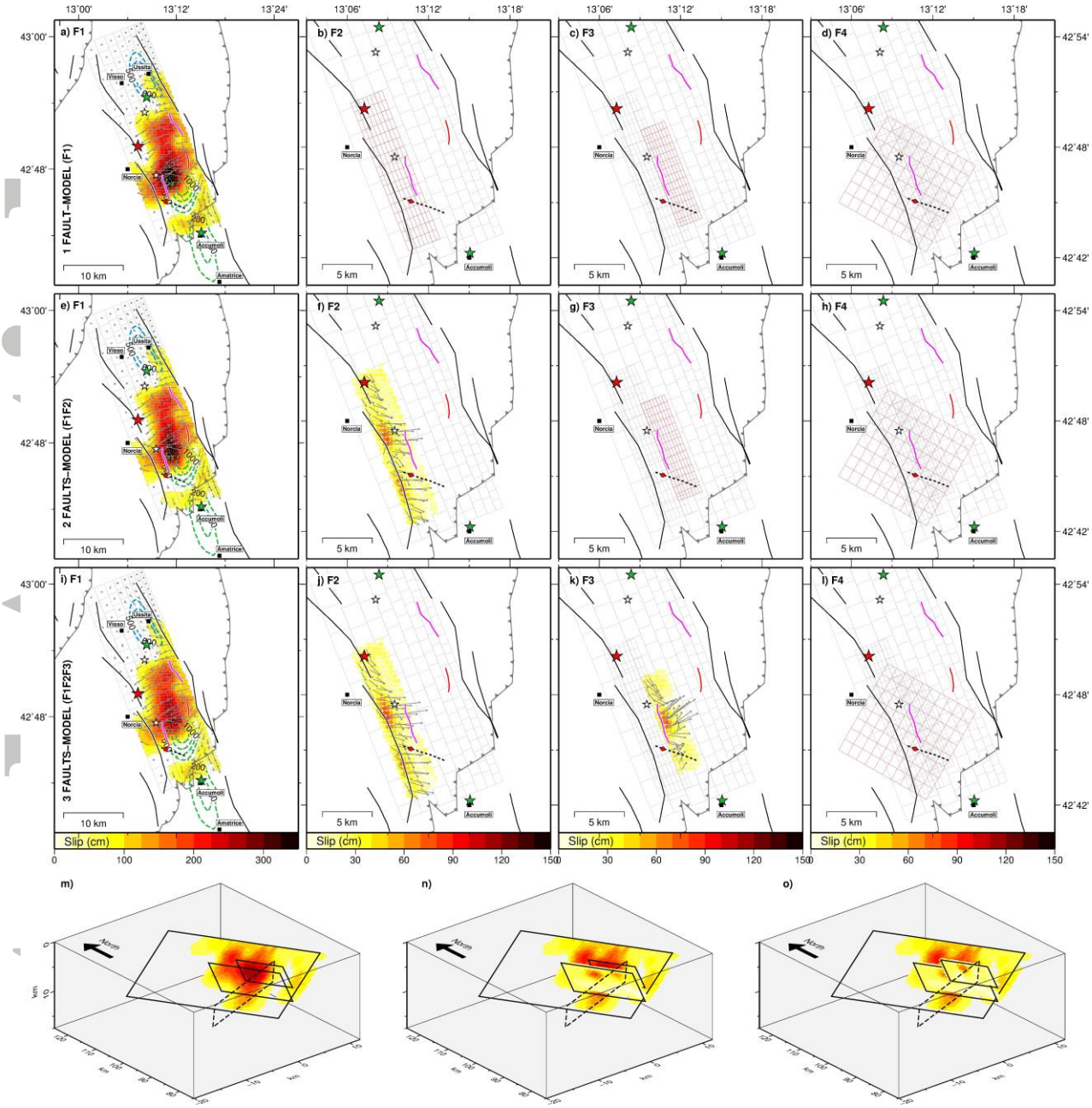

Figure 7. Coseismic slip models of the 30 October earthquake based on the half-graben rupture scenarios. Best-fitting models assuming slip on only segment F1 (a-d), on segments F1 and F2 (e-h), and on segments F1, F2 and F3 (i-l). The contouring (in mm) indicates the modelled slip distribution of the 24 August M_W 6.2 Amatrice earthquake (green dashed lines) and the coseismic slip of the 26 October M_W 5.9 shock (blue dashed lines) from *Cheloni et al.* [2017]. Other symbols as in Figure 1. For the best-fit 3-faults model, an oblique view of the model looking from above south-west is presented: (m) slip distribution on the master fault F1; (n) slip distribution on the master fault F1 and on the antithetic fault F2; (o) slip distribution on the master fault F1 and on both the two antithetic faults (F2 and F3). Note the different colour scale for slip distribution on fault F1 and on the antithetic faults F2 and F3, respectively. The black dashed fault plane represents the oblique dislocation (F4).

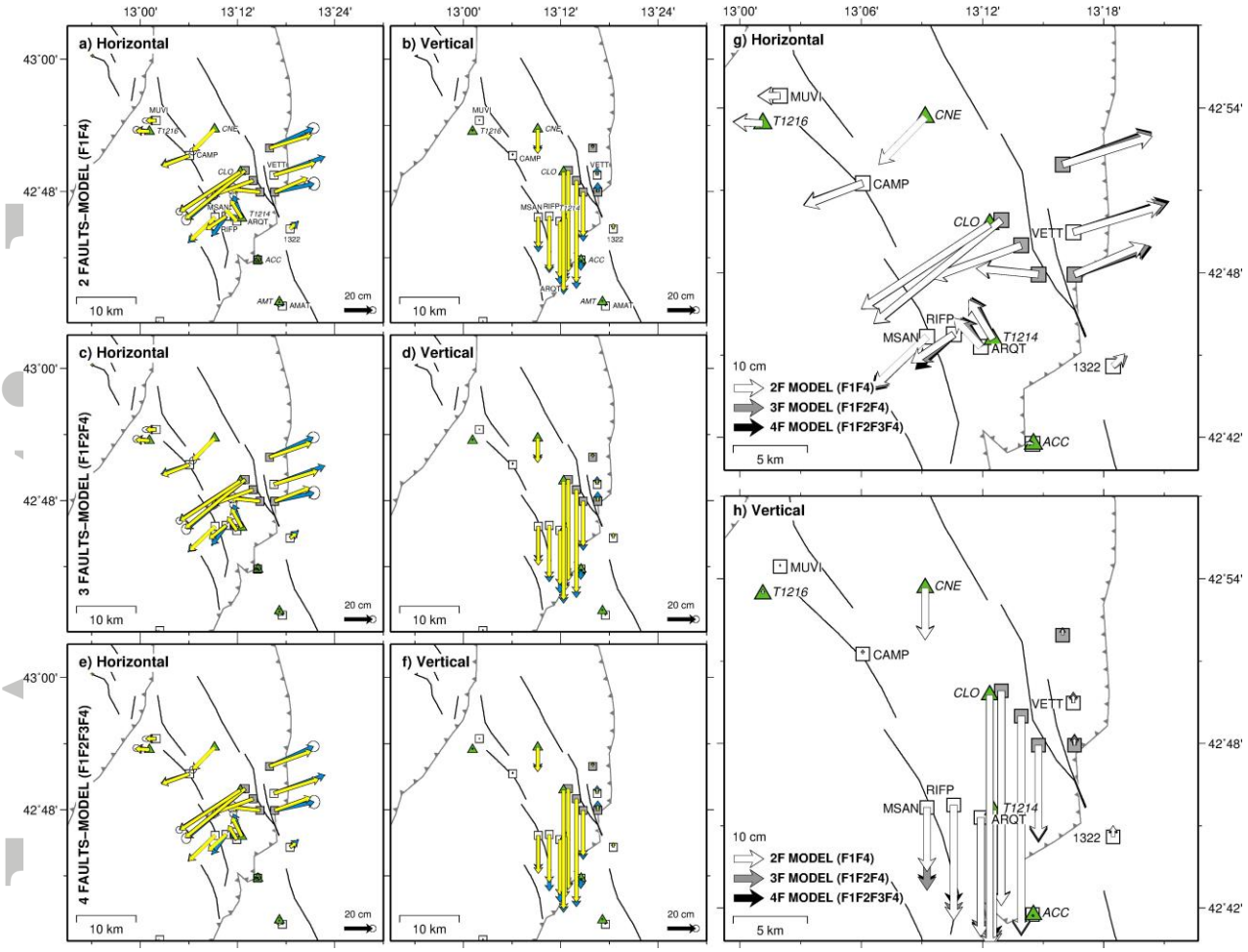

Figure 8. Observed and modelled GPS and SM-derived coseismic offsets based on the complex fault arrangement rupture scenarios including a transverse dislocation. Panels a-b, 2-faults model (F1+F4); panels c-d, 3-faults model (F1+F2+F4); panels e-f, 4-faults model (F1+F2+F3+F4). Observed (blue) and predicted (yellow) regional (white rectangles) and survey-mode (blue rectangles) GPS and SM-derived (triangles) horizontal and vertical displacements. The oblique low-angle segment F4 has an assumed fault dip angle of 36°. Panels g-h show the synthetic offsets from all of the different models (the displacements are shown by gray-scale vectors; white for displacement based on 2-faults model through to black for displacement based on 4-faults model). Other symbols as in Figure 1.

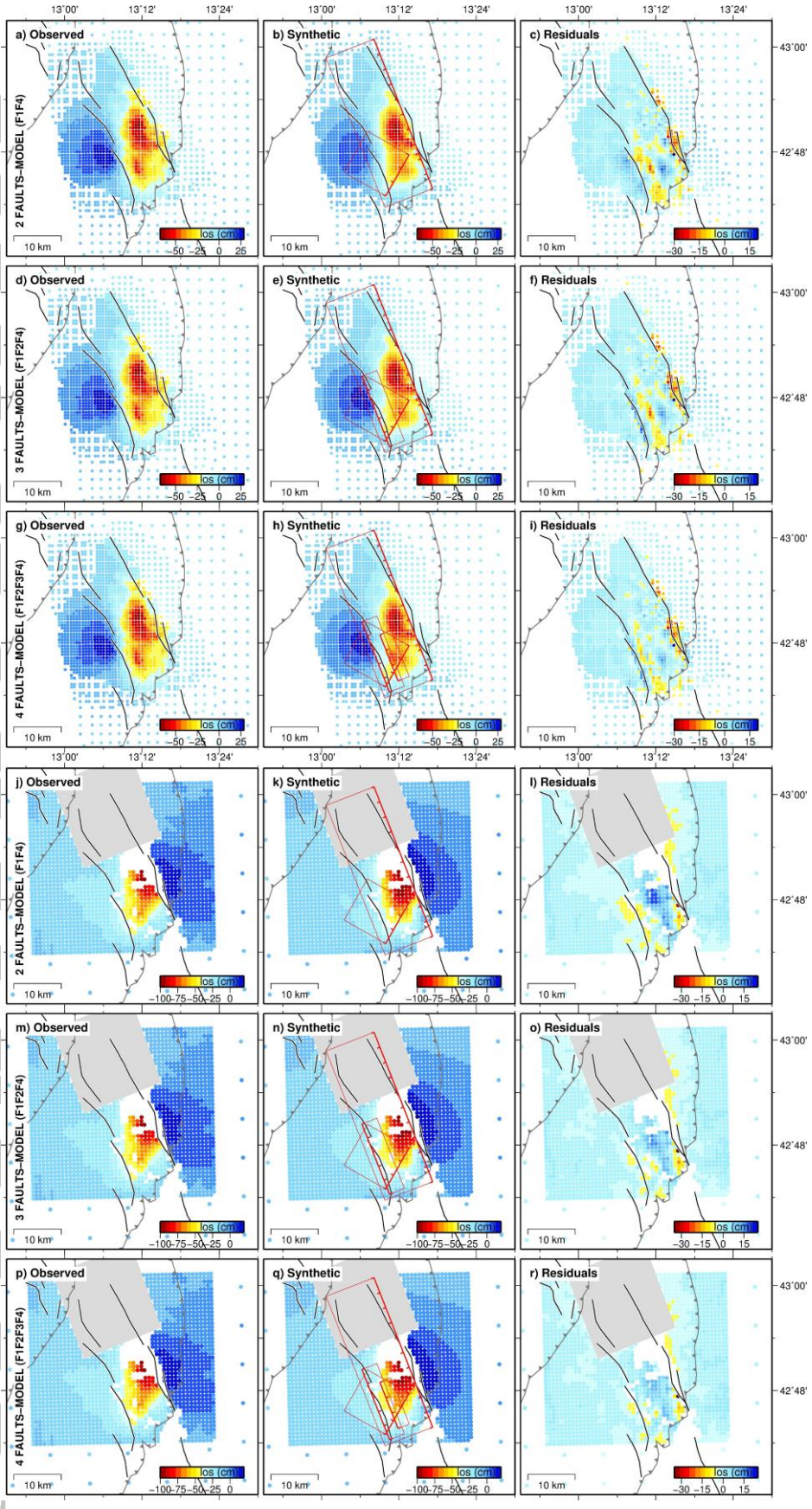

Figure 9. Observed, modelled and residual InSAR ALOS-2 ascending and SENT-1 descending unwrapped interferograms based on the complex fault arrangement rupture

scenarios including a transverse dislocation. Panels a-c and j-l, 2-faults model (F1+F4); panels e-f and m-o, 3-faults model (F1+F2+F4); panels g-i and p-r, 4-faults model (F1+F2+F3+F4). The red boxes indicate the fault segments modelled to have slipped during the earthquake in the different scenarios. The oblique low-angle segment F4 has an assumed fault dip angle of 36°. The gray area shows the cut of the northern part of the SENT-1 descending interferogram, that was affected by the 26 October Visso earthquake. Other symbols as in Figure 1.

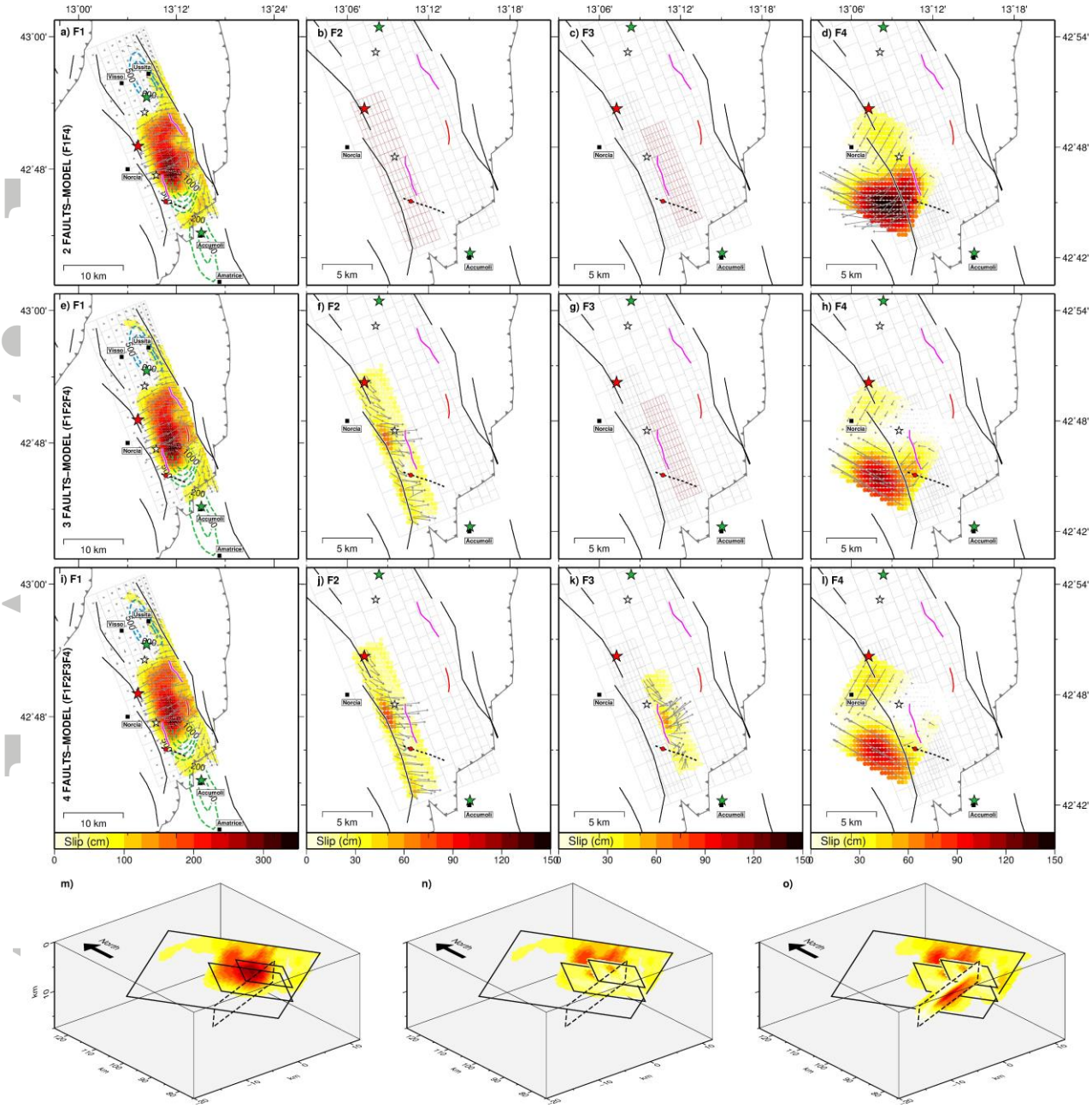

Figure 10. Coseismic slip models of the 30 October earthquake based on the complex fault arrangement rupture scenarios including a transverse dislocation. Best-fitting models assuming slip on segments F1 and F4 (a-d), on segments F1, F2 and F4 (e-h) and including all the segments, F1, F2, F3 and F4 (i-l). The oblique low-angle segment F4 has an assumed fault dip angle of 36°. The contouring (in mm) indicates the modelled slip distribution of the 24 August M_W 6.2 Amatrice earthquake (green lines) and the coseismic slip of the 26 October M_W 5.9 shock (blue lines) from *Cheloni et al.* [2017]. Other symbols as in Figure 1. For the 4-faults model, an oblique view of the model looking from above south-west is presented: (m) slip distribution on the master fault F1; (n) slip distribution on the master fault F1 and on the antithetic faults F2 and F3; (o) slip distribution on the master fault F1, on the two antithetic faults F2 and F3 and on the oblique dislocation F4. Note the different color scale for slip distribution on fault F1 and on the ancillary faults F2, F3 and F4, respectively. The black dashed fault plane represents the oblique dislocation (F4).

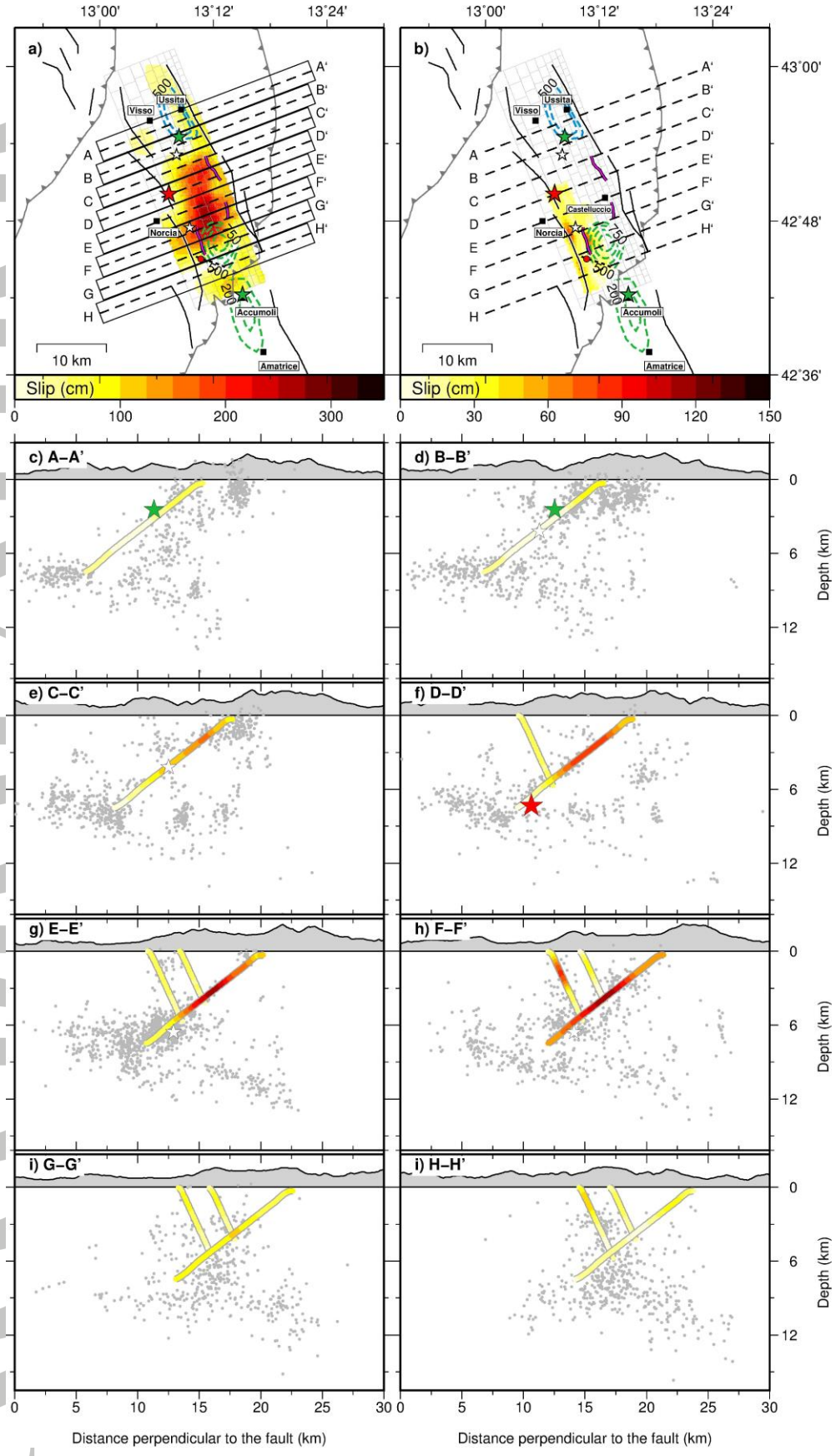

Figure 11. Best-fitting fault model for the 30 October earthquake. Our preferred fault array includes: (a) the main Mt. Vettore-Mt. Bove normal fault system (F1), and (b) the blind (F2)

and the Rifugio Perugia (F3) antithetic faults, respectively. The black boxes enclose the seismicity projected onto directions perpendicular to the strike of the modelled MVB fault system. The contouring (in mm) indicates the modelled slip distribution of the 24 August M_W 6.2 Amatrice earthquake (green lines) and the coseismic slip of the 26 October M_W 5.9 shock (blue lines) from *Cheloni et al.* [2017]. (c-i) Cross sections drawn perpendicular to the strike of the main fault, showing the position at depth and the amount of slip of our best-fit model, aftershocks (gray circles) and locations of the mainshocks (red star indicates the 30 October mainshock, green stars are the previous 24 August and 26 October events, while white stars are M_W>5.4 aftershocks).

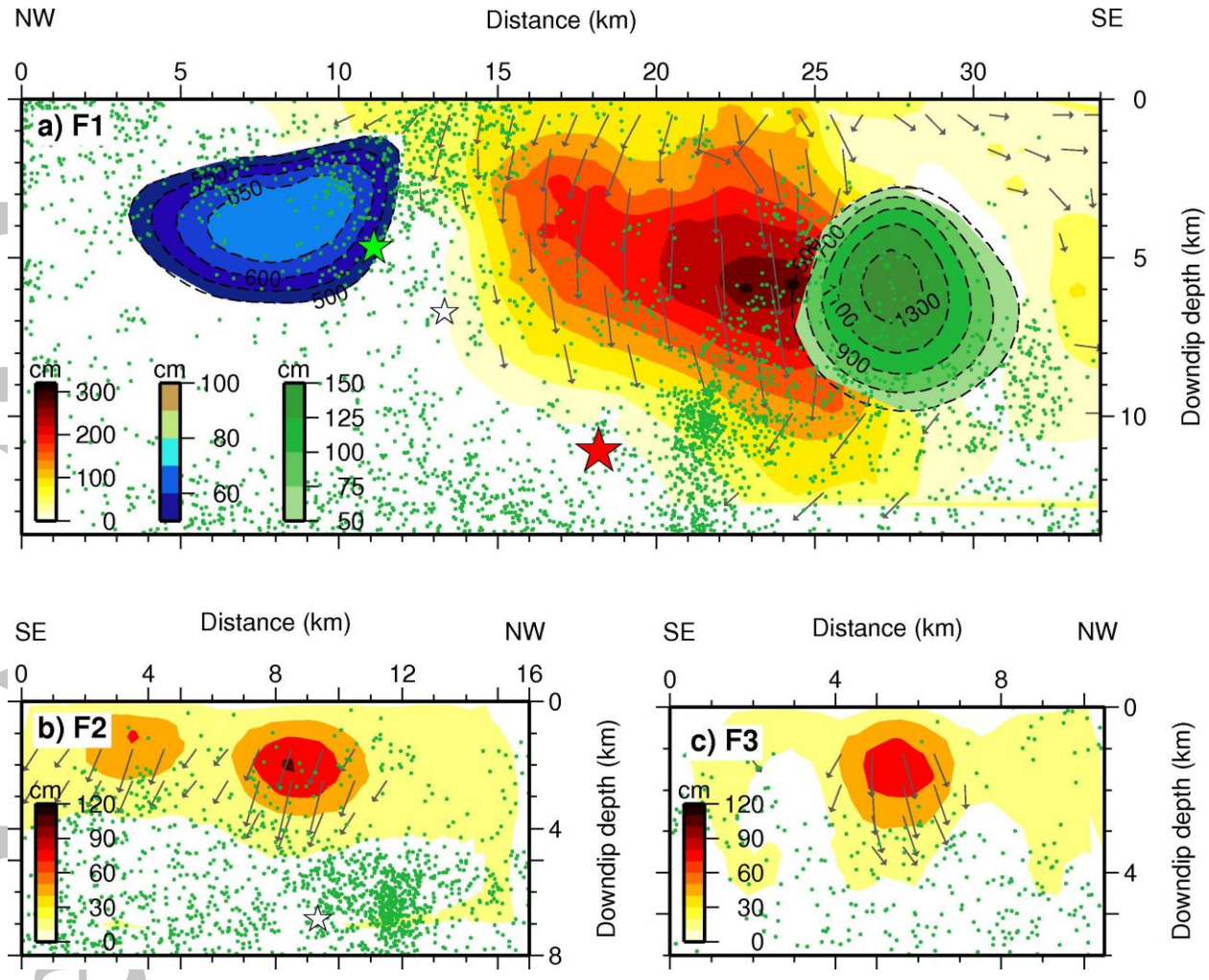

Figure 12. Geodetic model of the 30 October 2016 M_W 6.6 Mt. Vettore-Mt. Bove earthquake. Slip distributions on (a) the main Mt. Vettore-Mt. Bove normal fault system, (b) the blind and (c) the Rifugio Perugia antithetic faults, respectively. Seismicity: green dots are relocated aftershocks (between 26 October and 30 November) that occurred within 2 km on each side of the fault plane; red star indicates the 30 October mainshock, green star is the 26 October event, while white stars are M_W>5.4 earthquakes. Also shown in panel (a) the slip distributions of the previous 24 August M_W 6.2 Amatrice (green colors) and 26 October M_W 5.9 Visso (blue colors) earthquakes, respectively, from *Cheloni et al.* [2017], projected onto our best-fit fault plane.

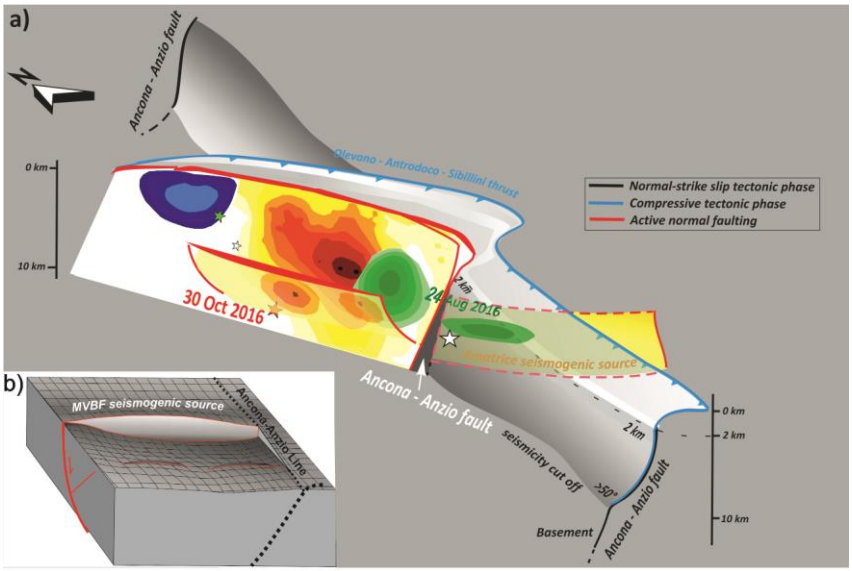

Figure 13. Structural scheme of the investigated area. (a) The red lines represent the major active fault strands and splays composing the MVB half-graben seismogenic source, while the light blue line is the inactive inherited compressive OAST ramp. The red star represents the 30 October mainshock, while the green and white stars are the 26 October and 24 August 2016 events, respectively. Also shown the slip distributions on the main MVB normal fault system relative to the three mainshocks of the 2016-2017 central Italy seismic sequence and on the main antithetic fault (color scale as in Figures 11 and 12). (b) Block-diagram showing the relationship between the MVB fault system and the inherited lithospheric discontinuity known as Ancona-Anzio Line (dashed black line).

Table 1. RMS of the model residuals after the joint inversion of the 30 October earthquake, by performing a number of inversions increasing the number of secondary fault segments in the half-graben rupture scenarios. The last column shows a 6-faults model that includes all the segments from the best-fit 3-faults model as well as other smaller synthetic and antithetic splays described in Section 4 (Fv, antithetic splay located near the Visso mainshock; Fp, Piano Perduto antithetic fault; Fs, hanging-wall synthetic splay). The last two rows of the table display the retrieved total seismic moment and moment magnitude.

Data type	**1-f model (F1)**	**2-f model (F1+F2)**	**3-f model (F1+F2+F3)**	**6-f model (F1+F2+F3+Fv+Fp+Fs)**
continuous GPS	2.1 cm	1.5 cm	1.4 cm	1.4 cm
survey-mode GPS	2.4 cm	2.1 cm	1.9 cm	1.2 cm
SM-derived	1.7 cm	1.2 cm	1.0 cm	1.0 cm
ALOS-2 asc	4.5 cm	4.0 cm	3.8 cm	3.6 cm
SENT-1 des	4.0 cm	3.2 cm	2.9 cm	2.9 cm
M_0 (10^{18} Nm) (tot)	11.4	11.6	11.7	11.7
M_W (tot)	6.67	6.68	6.68	6.68

Table 2. RMS of the model residuals after the joint inversion of the 30 October earthquake, by performing a number of inversions increasing the number of secondary fault segments in the complex fault arrangement scenarios. The last two rows of the table display the retrieved total seismic moment and moment magnitude. The F4 fault segment has an assumed dip angle of 36°. An alternative 4-faults model** includes instead an assumed high-dip angle of 70° of the segment F4.

Data type	**2-f model (F1+F4)**	**3-f model (F1+F2+F4)**	**4-f model* (F1+F2+F3+F4)**	**4-f model** (F1+F2+F3+F4)**
continuous GPS	1.6 cm	1.5 cm	1.4 cm	1.5 cm
survey-mode GPS	2.8 cm	2.2 cm	2.0 cm	1.9 cm
SM-derived	1.4 cm	1.2 cm	1.0 cm	1.0 cm
ALOS-2 asc	4.2 cm	4.0 cm	3.8 cm	3.8 cm
SENT-1 des	3.5 cm	3.1 cm	2.8 cm	3.0 cm
M_0 (10^{18} Nm) (tot)	11.1	11.4	11.5	11.7
M_W (tot)	6.67	6.67	6.68	6.68

Table 3. Best-fit 3-faults half-graben model source parameters of the 30 October earthquake. Longitude (lon) and latitude (lat) location refer to the center of the fault trace.

Fault name	**Lon (°)**	**Lat (°)**	**Strike (°)**	**Dip (°)**	**Length (km)**	**Width (km)**	**Mo (10^{18} Nm)**	**M_W**
Mt. Vettore-Bove (F1)	13.2114	42.8724	159.0	38.0	36.0	13.7	10.4	6.65
Norcia antithetic (F2)	13.1399	42.7731	339.0	65.0	16.0	8.0	1.0	5.96
Rif. P. antithetic (F3)	13.1746	42.7715	339.0	65.0	10.5	6.0	0.4	5.72